catalysts

MDPI

Review

Recent Manganese Oxide Octahedral Molecular Sieves (OMS–2) with Isomorphically Substituted Cationic Dopants and Their Catalytic Applications

Ferran Sabaté and María J. Sabater *

Instituto de Tecnología Química, Universitat Politècnica de València, Consejo Superior de Investigaciones Científicas, Av. Los Naranjos s/n, 46022 València, Spain; fersafor@doctor.upv.es
* Correspondence: mjsabate@itq.upv.es

Abstract: The present report describes the structural and physical–chemical variations of the potassium manganese oxide mineral, α–MnO_2, which is a specific manganese octahedral molecular sieve (OMS) named cryptomelane (K–OMS–2), with different transition metal cations. We will describe some frequently used synthesis methods to obtain isomorphic substituted materials [M]–K–OMS–2 by replacing the original manganese cationic species in a controlled way. It is important to note that one of the main effects of doping is related to electronic environmental changes, as well as to an increase of oxygen species mobility, which is ultimately related to the creation of new vacancies. Given the interest and the importance of these materials, here, we collect the most recent advances in [M]–K–OMS–2 oxides (M = Ag, Ce, Mo, V, Nb, W, In, Zr and Ru) that have appeared in the literature during the last ten years, leaving aside other metal–doped [M]–K–OMS–2 oxides that have already been treated in previous reviews. Besides showing the most important structural and physic-chemical features of these oxides, we will highlight their applications in the field of degradation of pollutants, fine chemistry and electrocatalysis, and will suggest potential alternative applications.

Keywords: manganese oxide; octahedral molecular sieve; cryptomelane; transition metal cation; isomorphic substitution; catalysis; heterogeneous

Citation: Sabaté, F.; Sabater, M.J. Recent Manganese Oxide Octahedral Molecular Sieves (OMS–2) with Isomorphically Substituted Cationic Dopants and Their Catalytic Applications. *Catalysts* **2021**, *11*, 1147. https://doi.org/10.3390/catal11101147

Academic Editor: Stanislaw Dzwigaj

Received: 30 July 2021
Accepted: 14 September 2021
Published: 24 September 2021

1. Introduction

Manganese is the third most abundant transition metal in the Earth's crust. It is commonly found in a wide variety of minerals, including carbonates (rhodocrosite, kutnahorite), oxides (birnessite, cryptomelane, hollandite, etc.), silicates (braunite, rhodonite) and sulfides (alabandite) [1,2]. Interestingly, iron is generally found in manganese deposits, so the pure phases of either of these two elements can be found in combination with the other at trace levels (as an impurity) [3]. Manganese can also participate in important biological functions at structural and metabolic levels (i.e., as a component of the bone structure, photosynthesis, etc.) [4,5], also being a very versatile element in the sense that it can be combined with other different elements to form interesting materials, such as oxides. In this case, a wide number of oxidation states (i.e., +2, +3, +4, +6 and +7) can be involved in these processes.

At the level of oxides, the three most abundant oxidation states for manganese that can be found in nature are +2, +3 and +4. In this regard, it is important to note that it is extremely difficult to find pure Mn oxides with a single oxidation state, provided that as a general rule, different oxidation states will usually coexist in the same structure [2]. As informative data, the three most prominent manganese oxide forms (MnO, Mn_3O_4 and MnO_2) have been applied in the fields of wastewater treatment [6–8], catalysis [9–14], supercapacitors [15–17], storage devices [18–21], medical agents [22–24], etc.

Among these oxides, manganese oxide (IV), MnO_2, is probably one of the most important oxides since it has important physical–chemical properties, such as an easily

exchangeable multiple oxidation state, a thermally stable structural form, a high grade of polymorphism and low cost and benignity with the environment [25–28].

In general, the different forms for MnO_2 can be obtained from different synthetic routes (sol–gel, precipitation, ionic–exchange, etc.), by varying the precursor salts and also by using templates or structure-directing agents (i.e., glucose, hexadecyltrimethylammonium bromide, etc.). For many years, and due to the increasing importance of MnO_2 in the manufacture of electronic devices, more precise and sophisticated synthesis methods [29–31] have appeared in order to obtain oxides with specific and prominent characteristics. In this regard, the large number of MnO_2 polymorphs—as well as their multivalent nature and nonstoichiometric composition—makes their classification difficult [32]. Consequently, the catalytic activity of these oxides will rely on their chemical composition, their crystallographic structure and parameters such as pore structure (size and type), morphology, etc.

Taking these considerations into account, in Table 1, we have included the most important allotropic forms of MnO_2 and their structural properties. Most of them can be obtained through a hydrothermal redox process from different manganese precursor salts [33,34]. We must indicate that the information included in Table 1 (i.e., formula and manganese oxidation state) refers to general data which can undergo modifications depending on small synthetic variations.

Table 1. Main MnO_2 forms and their basic structural characteristics. Adapted from References [15,19,33,35–42].

Form	Name	Formula	Space Group	Structure ($m \times n$, Dimension Tunnel Structure)	Cell [a]	Oxidation States of Mn
α–MnO_2	Hollandite	$Ba(Mn^{4+}{}_6Mn^{3+}{}_2)O_{16}$	Tetragonal/monoclinic *I*4/m	(2 × 2) tunnel	hcp	+4, +3
β–MnO_2	Pyrolusite	$Mn^{4+}O_2$	Tetragonal, $P4_2/mnm$	(1 × 1) tunnel		+4
γ–MnO_2	Nsutite	$(Mn^{4+},Mn^{2+})(O,OH)_2$	Hexagonal/Orthorombic, (n.d.)	(1 × 1)/(1 × 2)		+4, +2
R–MnO_2	Ramsdellite	$Mn^{4+}O_2$	Orthorombic, *P*nma	(1 × 2) tunnel		+4
ε–MnO_2	Akhtenskite	$Mn^{4+}O_2$	Hexagonal, $P6_3/mmc$	dense		+4
δ–MnO_2	Birnessite	$Na_{0.5}(Mn^{4+}Mn^{3+})O_4 \cdot 1.5H_2O$	Monoclinic, $P6_3/mmc$	(1 × ∞) layer	hcp/fcc	+3, +4
λ–MnO_2	Spinel	$(Li)Mn_2O_4$	Spinel, *F*d3m	(1 × 1) tunnel	fcc	+3, +4

[a] hcp: hexagonal close-packed, fcc: face-centered cubic.

All the structures included in Table 1 have MnO_6 octahedral units as common structural building blocks, so that depending on the disposition and interrelation between them, different structures will emerge. Some authors [19] tend to classify these oxides according to the way these units connect and interrelate with each other (i.e., tunnels, layers, etc.). For example, δ–MnO_2 materials have [MnO_6] shared edges in each layer, with cations (e.g., K^+, Li^+, Na^+, etc.) and water molecules occupying interlayer positions. On the other hand, in tunnel structures, the disposition of [MnO_6] gives rise to a wide range of tunnel sizes, for example: β (1 × 1), γ (1 × 2 and 1 × 1), α (2 × 2), etc. (see Section 2).

In parallel, the tunable redox properties of MnO_2 and the mobility of labile lattice oxygen make these oxides powerful catalysts in important catalytic reactions, such as oxidations. As will be shown later in more detail (see Sections 2.2 and 2.3), the presence of mixed Mn oxidation states can be quantified, giving rise to an interesting parameter known as average oxidation state (AOS) [43].

Chemical titration methods (i.e., thiosulfate or potential voltametric titrations), magnetic measurements and spectroscopy techniques (i.e., Raman, XPS) have been widely applied in order to obtain such AOS values [43–46]. Interestingly, the great variety of oxidation states that can be modified on purpose (by means of synthetic strategies) offer a

wide range of applications. However, it is rather difficult to correlate the distribution of Mn species with catalytic activity, because unexpected factors such as the presence of oxygen vacant defects (OVDs) can play an important role in catalysis, given that these effects are not a priori easily predictable.

Currently, it is possible to divide the application fields of MnO_2 oxides into two groups: (i) fine chemistry (i.e. synthesis of lactones, aldehydes, etc.) [47–54] and (ii) sustainable chemistry and environmental remediation, involving highly interesting reactions such as oxygen-evolution reaction (OER), VOC degradation, syngas reactions, biofuel production, etc. [26,55–59]. For this reason, manganese oxide-based materials are the subject of intense research, in particular layered and porous tunneled structures have received significant attention due to their excellent catalytic activity and especially from their potential implementation in energy-related topics.

In view of these precedents, our aim has been to offer the reader a comprehensive survey on design, synthesis, characterization, and applications of nanostructured MnO_2, in particular octahedral molecular sieves (OMS), as catalytic functional materials during the last ten years. The synthesis and description of their porous tunneled or layered structures and related materials will be also addressed. We will show that right now, this an active field of research, and will provide final conclusions on the topic as well as future trends.

2. Octahedral Molecular Sieves (OMS)

2.1. General Aspects

Molecular sieves are, generally speaking, microporous solids with very narrow and uniform porosity, so that, depending on their porous dimensions, they can be divided into different categories: microporous (<2 nm), mesoporous (2–50 nm) and macroporous (>50 nm). This general classification also includes different types of aluminosilicates (i.e., zeolites, etc.) with tetrahedral building units which have been involved for years in industrial processes such as purification, separation, petroleum refining and other catalytic reactions [60–69]. Along with these aluminosilicates, there are octahedral molecular sieves (OMS), which consist of the assembly of octahedral MnO_6 building units interconnected through oxygen atoms [70], showing an unprecedented versatility in terms of redox properties, arrangement and doping possibilities with respect to other materials or building systems [63,71,72]

2.2. Manganese Octahedral Molecular Sieves

Most of these materials were reported by Suib et al. during the 1990s [73–78], and they quickly attracted the attention of the scientific community due to their promising applications, especially at the level of electrochemistry and catalysis. This trend can be clearly confirmed in Figure 1.

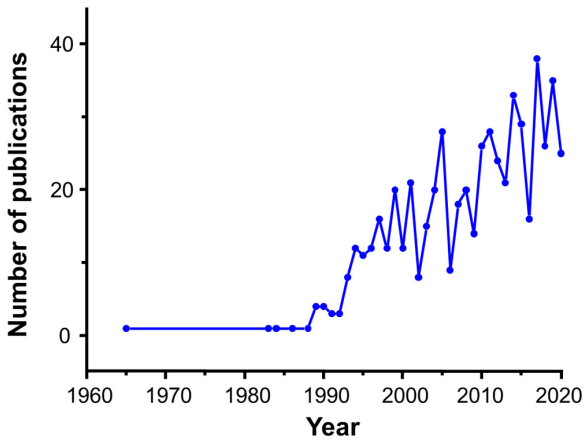

Figure 1. Evolution of number of publications containing references to OMS materials. Source: Compilation based on Scopus data (March 2021).

For those readers interested in deepening their preparation and physical–chemical characteristics, we suggest some useful references [34,74,75,79,80].

As previously advanced and continuing with the structural description of these materials, the arrangement of octahedral MnO_6 units will define the oxidic structure that can potentially be obtained, in particular tunnel structures with dimensions ranging from (2.3 × 2.3) Å to (4.6 × 11.5) Å [81]. All these tunneled conformations are named according to their mineral of origin and will be labeled as a function of their tunnel dimensions as $m \times n$, where m and n are the octahedral units arranged in each of the directions.

Some known examples are rutile (1 × 1), ramsdellite (2 × 1), hollandite (2 × 2), romanèchite (3 × 2) and todorokite (3 × 3). As it occurs with the respective source minerals, tunnels usually contain water molecules and/or alkali and alkaline earth cations in order to maintain the electrovalence of the system and give stability to the tridimensional structure. It is important to indicate that pioneering studies [81] were focused on obtaining larger tunnel dimensions in order to expand the number of applications, including their use as cation exchangers such as zeolites [79,82].

Curiously, from a crystallographic point of view, and under the hypothetical and unlikely situation that tunnels are empty, different correlations can be established in some cases between the above-cited structures. As an example, Figure 2 shows the possibility of easily transforming a 1 × 1 structure (rutile) into a 2 × 2 structure (hollandite) by means of a 45° rotation of octahedral units.

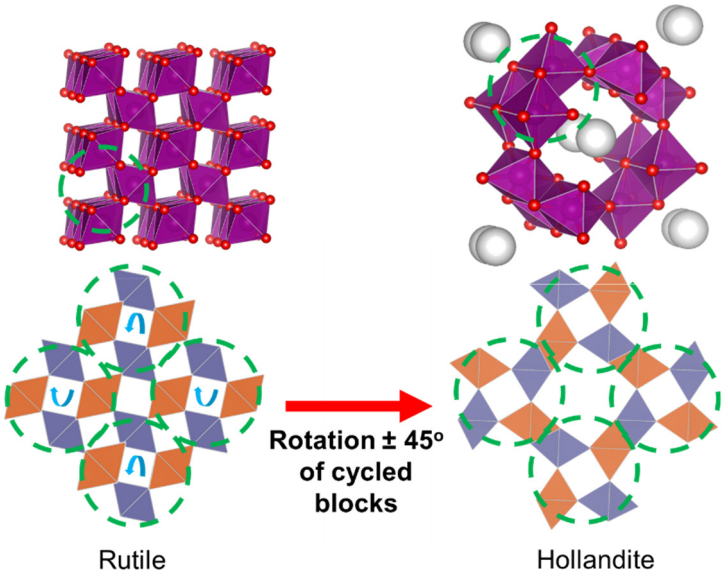

Figure 2. Scheme for the transformation of rutile into hollandite by rotating the blocks enclosed in a circle clockwise or counterclockwise (turn indicated by the blue arrows). As an explanatory note, orange octahedral units are placed in a different plane with respect to blue units. Adapted from [83].

Indeed, when looking closely at Figure 2, it is possible to observe how the shared vertices of octahedral units in the rutile structure will easily share faces in the hollandite structure so that the original stoichiometry can be maintained. Therefore, though the mobility of atoms is very restricted, it is possible to appreciate the existence of a common denominator for all the structures, suggesting that these materials present a sort of "memory effect" [83–85]. This would explain why some little modifications in the original oxide can lead to the appearance of so many different structures and/or segregated phases, such as psilomelane, ramsdellite, etc.

On the other hand, the fact that all these OMS systems present mixed manganese oxidation states (mainly Mn^{4+} and Mn^{3+}, and occasionally Mn^{2+}) is very striking, and this results in an average oxidation state (AOS) of ~3.8 for these materials. In this regard, since different microporous systems with different AOS values can be achieved, they will present

a rather unusual and unique combination of porosity and semi-conductivity properties [78] within the field of molecular sieves.

These amazing properties explain why these materials have been largely explored in different areas of chemistry (Figure 1). Indeed, catalytic properties of OMS materials have been shown to be related to the redox cycling of certain oxidation states of manganese (i.e., Mn^{2+}, Mn^{3+} and Mn^{4+}), where electron transfer ability seems to have a crucial role [34]. This important feature was widely studied using specific electrochemical techniques by De Guzman et al. [86].

It should be noted that the nomenclature for these materials follows the code: "OMS–number". As an example, one of the most important OMS materials with catalytic applications is OMS–1. It is closely related to the mineral todorokite, that has the formula $T_2Mn_4^{2+}O_2^{4+}{\cdot}9H_2O$ (T = Cu, Ni, Zn, Mg, Co) [87], and it has a 3 × 3 tunnel structure (6.9 Å × 6.9 Å).

OMS–1 has been used both in its original form and doped with other transition metals, being applied as a cation exchanger [88] and as a catalyst in CO_2 methanation processes [89], steam reforming [90], degradation of pollutants [91], electrocatalysis [87] and energy storage [92–94], among other reactions.

In this context, the most extensively studied OMS-type Mn oxide is most likely the cryptomelane-type oxide, OMS–2, as shown in Figure 3.

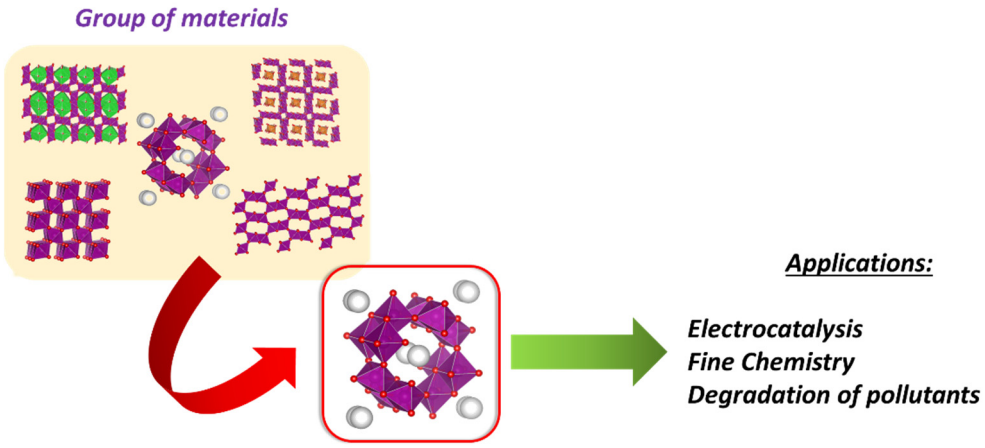

Figure 3. Most representative applications of nanostructured cryptomelane OMS–2.

For this reason, we will focus on metal-doped OMS–2-type oxides, describing their structure in detail, as well as their physical–chemical properties and applications of interest.

2.3. Cryptomelane (OMS–2)

2.3.1. General Aspects

Cryptomelane is a manganese oxide composed of edge-shared octahedra of MnO_6 units, forming a 2 × 2 (0.46 × 0.46 nm) tunnel structure (Figure 4). The size of these tunnels is ca. 6.4 Å (35% smaller than those of OMS–1).

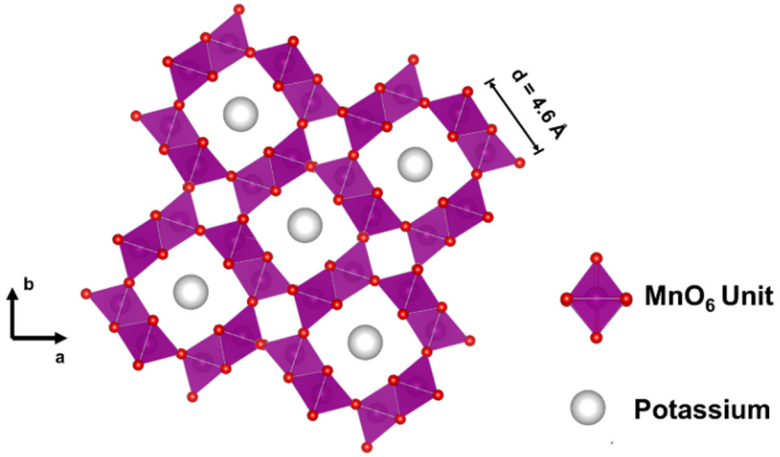

Figure 4. Schematic representation of the crystal structure of K–OMS–2. Cell dimensions are indicated.

The general chemical composition of OMS–2 oxide is $A[Mn_8O_{16}]\cdot nH_2O$, where Mn^{2+}, Mn^{3+} and Mn^{4+} cations are arranged in different structure sites, resulting in an average oxidation state (AOS) of approximately +3.8. Counter cations located in the tunnels (A) will compensate the charge imbalance of the system. In this context, Mn oxide will receive a particular name depending on the charge compensating cation located in the tunnels: hollandite (Ba^{2+}), cryptomelane (K^+), manjiroite (Na^+) and coronadite (Pb^{2+}). All these names come from their respective mineral of origin. In this review, we focus on cryptomelane, and from now on this material will be named as K–OMS–2.

As mentioned above, OMS–2 has a 2 × 2 tunnel structure, which is built by edge and corner sharing [MnO_6] octahedral units, leading to different pore sizes. OMS–2 has a mixed valent manganese framework with a higher amount of Mn^{4+}. Besides, K^+ ions are located in the tunnels and can be exchanged by other inorganic cations [95]. For example, K^+ can be exchanged by protons (H^+), H–K–OMS–2 when K–OMS–2 is treated with a diluted acidic solution (e.g., HNO_3), while heating with vigorous stirring [96,97]. Obviously, metal cations can also be incorporated into the tunnels through a partial substitution of original potassium cations (i.e., cobalt, copper, palladium, ceria, iron, etc.), resulting in variations in some parameters such as porous volume and surface area. It is important to note that this process can imply deep structural changes in the tunnel structure or even lead to the collapse of the structure due to differences between the ionic radii of K^+ and the cationic dopant. All these features will induce changes in the catalytic activity [98–103]. As an example, Section 3.1.2 will illustrate this point taking the [Ce]–K–OMS–2 materials as an example.

On the other hand, it is important to remark that doping into tunnel positions is disfavored when the cationic dopant radii is similar in size to Mn, since the cationic dopant (M) can compete with Mn to obtain a VI-fold site in the framework of OMS–2 material [104–108].

With respect to the synthesis process, it is important to indicate that a wide range of synthetic methods have been described for the synthesis of OMS–2 oxides, although a rather general method consists of mixing a manganese precursor salt (i.e., manganese(II) sulphate, manganese chloride(II), etc.) in acidic medium, and potassium permanganate ($KMnO_4$) as an oxidant agent [34].

In this context, sol–gel, hydrothermal, microwave, phase-transfer, solvent-free and reflux methods have been reported for their synthesis [79,81,109–113]. Slight modifications in the synthetic procedure can led to noteworthy changes in the final solid, such as: morphology, reactivity, textural properties, etc.

For example, it has been reported that surface area values are closely related to the synthetic method [114]. Indeed, Figure 5 shows that more sophisticated synthetic methods can lead to enhance the surface areas (up to 7 times) and to a shortening of crystallization time.

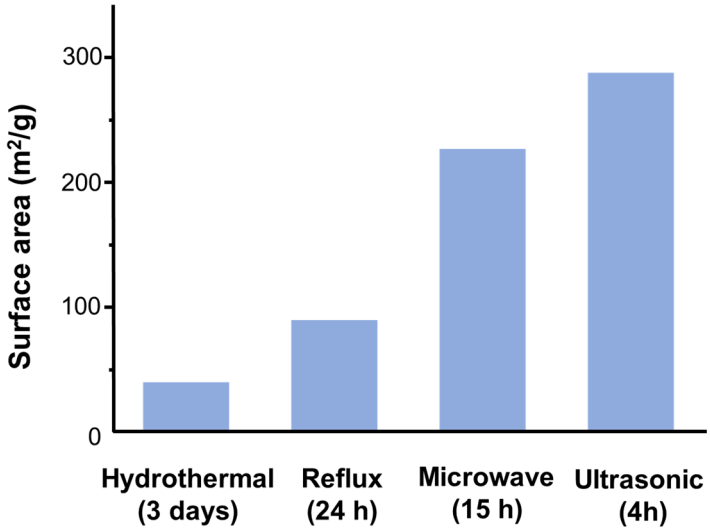

Figure 5. Influence of synthetic methodology on the surface area value (N_2, 77K) obtained for pure K–OMS–2. The synthesis time is indicated in parenthesis. Data are obtained from [114].

Although these materials usually present a needle-like shape with a length between 30 and 1400 nm and an internal diameter of ca. 10–30 nm (Figure 6b,c), higher values can be achieved under specific synthesis conditions [115].

Nonetheless, in all cases, the K–OMS–2 morphology will always be nanorods (or "needle-like") (Figure 6a). At this point, it is interesting to highlight that the dimensions of these solids can be controlled a priori using different additives during the synthesis.

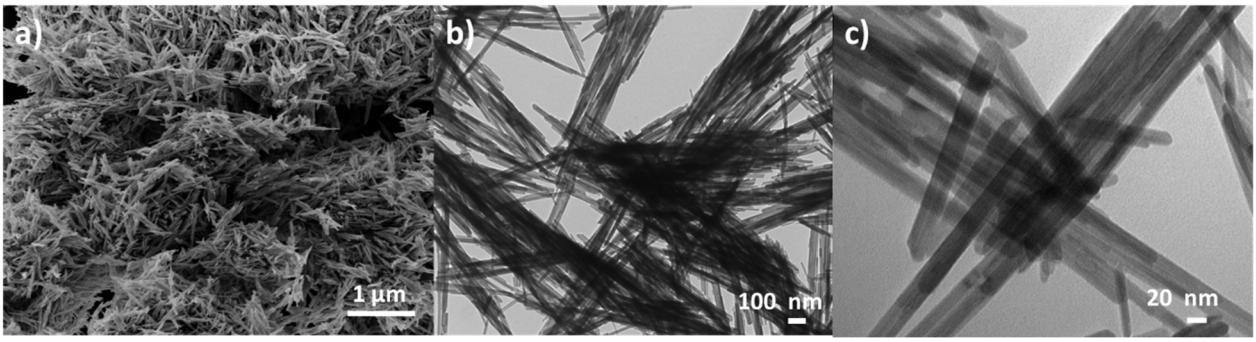

Figure 6. SEM image (**a**) and HR-TEM images (**b**,**c**) of pure K–OMS–2 material (unpublished results).

As an example, Liu et al. [107] reported that K–OMS–2 could be obtained with controlled particle sizes varying from 8.2 to 61.1 nm in width and from 35.6 to 1376.1 nm in length by reacting $KMnO_4$ with different carboxylic acids [107].

2.3.2. Assessment of Doping Processes

As previously stated, OMS–2 material is an environmentally benign and relatively cheap manganese oxide with a wide range of interesting applications in the fields of environmental and sustainable energy [55,116–120], electrocatalysis and energy storage [121–125], as well as catalysis for fine chemistry [112,126–133]. As previously indicated, the wide variety of structures that OMS–2 oxide can adopt makes it easy for these materials to adjust to each specific application. Indeed, depending on the reaction and morphology of the oxide, the catalytic activity can be optimized in each particular case.

In this respect, there is a way to influence the catalytic activity that consists of incorporating a second metal transition element in the K–OMS–2 structure through doping, whereas alternative synthetic strategies have also moved to other unexplored fields to modify their activity. For example, by combining K–OMS–2 with biopolymers such as chitosan to obtain the Fe_3O_4@K–OMS–2@CTS catalyst [134], or by combining with silicates SiO_2 to obtain K–OMS–2/SiO_2 materials [135].

Thus, returning to the topic of doping, the incorporation of a second metal ion by means of a doping process can take place on the surface, in the tunnels or in the structure (Figure 7).

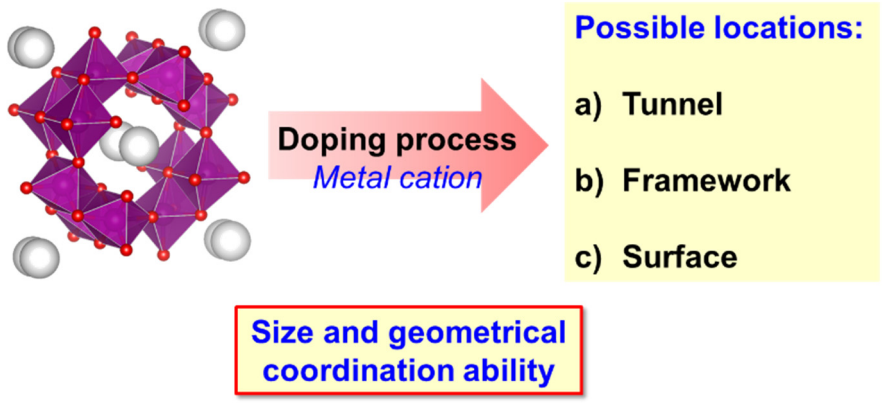

Figure 7. Scheme of the available positions for the cationic doping process on K–OMS–2 materials.

The definitive location will be closely linked to the synthesis procedure, and more specifically, to the size and geometrical coordination ability of the cationic dopant (Figure 7).

Doping processes are clearly used to tune the structure, morphology and lattice parameters in order to provide novel chemical and physical properties to the solid. In this line, structural defects, active metal species derived from doping [136–138] and oxygen vacancies [105,139,140], together with unexpected synergic effects [132,141], will define the true performance of the materials in catalytic reactions.

In this case, the review will focus on doping processes at the level of framework. This doping method usually involves the replacement of manganese ions by isovalent transition metal cations that will act as dopants, being denoted as the isomorphic substitution process.

The isomorphic substitution is not exclusive of these materials, provided that other different molecular sieves (i.e., zeolites) can undergo isomorphic substitution at the level of Si tetrahedral building units using pre- and post-synthetic procedures [142,143].

In this case, the most efficient synthetic strategy to achieve an isomorphic substitution is the incorporation of the dopant agent from the beginning of the synthesis, which consists on adding the metal salt precursor to a solution of starting manganese salts. Proceeding in this way, the time contact between manganese/cationic dopant species increases during the comproportionation step, and the introduction of the latter into the structure is favored.

After the doping process, the characterization of these materials will be crucial in order to confirm the structure of the oxide as well as the location of the doping cation. For this purpose, two different types of characterization techniques can be applied depending on what type of information can be extracted. First, (i) techniques that allow the direct

confirmation of the position of the cation in the structure (i.e., atomically resolved transmission electron microscopy, X-ray absorption spectroscopy), and (ii) techniques that allow knowing the exact or precise position of the cation indirectly (i.e., Raman and UV-visible spectroscopy, ICP analysis, etc.) and that must be applied together to characterize the solid. The choice of one group of techniques or another will depend on the availability and accessibility to relevant instrumentation or equipment and their own limitations of each of these techniques.

For example, within the field of electronic microscopy, neutron diffraction and atomically resolved transmission electron microscopy allowed to elucidate the precise localization of Fe and Ti cations in metal-doped OMS–2 materials. In this regard, González-Calbet et al. [144] proposed the unequivocal location of Fe and Ti cations in manganese hollandite nanowire materials, [Fe]–K–OMS–2 and [Ti]–K–OMS–2, using neutron diffraction and atomically resolved transmission electron microscopy. We must highlight that this is the first study where [Ti]–K–OMS–2 has been reported by observation on an atomic scale (Figure 8). Therefore, these studies confirm that advanced techniques provide valuable and unambiguous information on cationic dopants as well as on oxygen vacancies locations in K–OMS–2 materials.

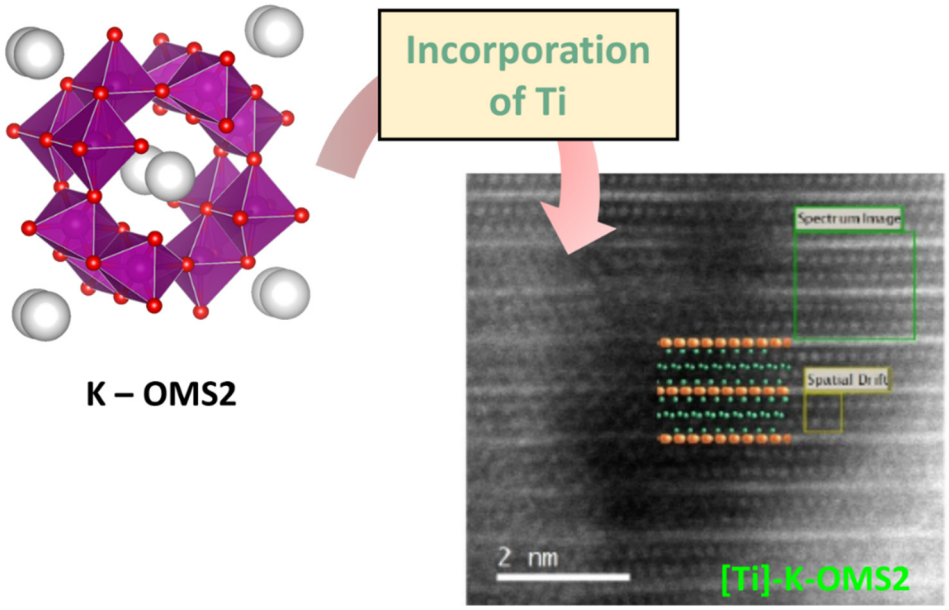

Figure 8. Scheme of Ti species into K–OMS–2. HAADF images (extracted from [144]) along the [111] zone axis, indicating the area where the spectrum image was acquired. A schematic representation of the structure is also included. The area of the image used to automatically avoid spatial drift of the sample during Dual EELS acquisition is also marked [144].

On the other hand, and as previously stated, there is a second way to determine the position of a doping cation by means of indirect methods, which will ultimately reveal that isomorphic substitution processes have been successful.

This last method requires a large number of tests to ensure that the cation has been incorporated into the structure. For example, from X-ray powder diffraction (XPRD), the expansion/contraction of cell parameters can be confirmed [104], given that when transition metals are incorporated into the structure, they can induce deformations of structural parameters (i.e., bond distances, angles, etc.). Moreover, when the doping metal cation content is high enough, changes in the morphology of particles can occur, leading to the collapse of the structure [145,146]. In this context, morphological changes can be observed directly by electron microscopy (SEM, TEM).

X-ray absorption spectroscopy (XAS) can also shed light on the disposition of manganese atoms and their local environment (dopant cations, oxygen vacancies, etc.) [147]. Besides, Raman spectroscopy can also provide information about the local environment around a metal cation through variations in the Mn-O strength in a semi-quantitative way by applying the Hook's law [108,139]. Similarly, UV-visible spectroscopy allows us to identify the main absorption bands and calculate the optical band gaps (E_g) [148,149]. This last parameter will experience modifications from undoped to doped materials if the level of incorporation of the dopant is significant [108].

On the other hand, chemical composition analyses, such as inductively coupled plasma (ICP) and energy-dispersive X-ray spectroscopy (EDX), can provide experimental values about the chemical composition. Then, they can be used to compare the expected isomorphic substitution [108,146] with the aid of crystallography models proposed for cryptomelane structures [150,151].

Other techniques that can shed light on the successful incorporation of cationic dopants in the cryptomelane structure are temperature programmed desorption (TPR) and cyclic voltammetry (CV). Unfortunately, the multiple oxidation states of Mn along with its renowned conductivity can hinder the characterization of OMS–2 materials, for example through electron paramagnetic resonance (EPR). In addition, the intense black color of the samples makes IR measurement often not feasible due to the transmission acquisition becoming more cumbersome [108].

In this regard, the influence that isomorphic substitution exerts at certain positions will be the most decisive proof of the benefit that doping has on certain catalytic reactions. For this reason, in this review, we describe the structural and physical–chemical variations due to doping of [M]–K–OMS–2 cryptomelane materials (where M indicates the cationic dopant agent) as well as the influence that this modification has in catalysis.

This review will encompass the series of [M]–K–OMS–2 oxides reported during the last 10 years, allowing us to provide a general view of the different fields where they can be applied. We highly recommend some sources [34,146,152] that cover in depth the syntheses and structural characterization of the first reported [M]–K–OMS–2 materials.

3. [M]–K–OMS–2 Materials

3.1. Characterization Data

This section collects typical chemical, structural, morphological and textural parameters related to isomorphic substituted materials reported in the literature during the last decade. Older isomorphic substituted materials, [M]–K–OMS–2, that have been included in previous related reviews will not be treated here [146,152]

Then, we will describe high-impact catalytic applications (e.g., CO oxidation reaction, degradation of pollutant agents and synthesis of fine chemical products) of cryptomelane [M]–K–OMS–2 oxides, and when appropriate, we will make a comparison between them. Table 2 summarizes the most important features of the most recently reported [M]–K–OMS–2 isomorphic materials. For more information on In-, Zr- and Zn-doped oxides, we suggest going directly to the respective monographs included in this review. Similarly, when the reader wants to look deeper at a certain material, we highly recommended to go to the references included in their respective sections.

Table 2. Chemical composition and textural information of [M]–K–OMS–2 materials.

Metal Incorporated into the Framework	Synthesis	Composition Range (% wt.)	Surface Area Range, N_2, 77K (m^2/g)	Morphology	Reaction Examples	References
Ag	Hydrothermal, reflux, microwave assisted, solid state	0–2	80–160	Nanorod (50 nm–1 μm)	CO oxidation	[153,154]
Ce	Reflux	0–8	72–200	Nanorod (500 nm)	VOC and ozone degradation	[106,155,156]
Ru	Reflux	0–4	84–131 [a]	Nanorod (150–500 nm)	Oxidation of alcohols	[108,133]
Ti	Reflux	0–2	152–155	Nanorod (n.a.)	Oxidation of styrene	[157]
Mo	Reflux	0–10	100–210	Nanorod (50–200)	CO oxidation	[150,158]
W	Reflux	0–10	110–190	Nanorod (50–200)	CO oxidation	[151]
V	Reflux	0–10	120–190	Nanorod (50–200)	CO oxidation	[159,160]
Nb	Reflux	0–30	147–220	Nanorod (51–184)	Oxidation of methanol	[161,162]
In	See Sections 3.1.6–3.1.8					
Zn						
Zr						

[a] CO_2 surface area value, in accordance with the procedure described in [163].

3.1.1. [Ag]–K–OMS–2

One of the first examples of isomorphically substituted cryptomelane materials described in the literature corresponds to Ag-doped K–OMS–2 ([Ag]–K–OMS–2) [153], which was reported in 2007, and for this reason it should not be included a priori in this review. Nevertheless, since the most important features of this oxide were not elucidated until recently, we finally decided to include it along with the rest of the most recently reported doped oxides.

The XRPD pattern for [Ag]–K–OMS–2 material unequivocally showed the typical characteristic peaks belonging to the cryptomelane phase (JCPD #00-029-1020), that is 2θ = 12.6°, 17.9°, 28.7°, 37.5°, 41.9°, 49.9° and 60.1°. No other additional peaks were found in the diffractogram, as usually occurs for [M]–K–OMS–2-doped oxides. This fact evidenced that no segregated phases were formed, and on the other hand, that there had been no changes in the structure either.

In the same line, SEM and TEM micrographs showed that no morphological changes had taken place, hence giving support to what was observed by XRPD (Figure 9) [153].

Adsorption–desorption isotherms and pore size distribution showed that both Ag-doped and undoped (K–OMS–2) materials had a type-II isotherm, which is typical for macroporous and non-porous materials. The isotherm plots showed a steep increase in the low relative pressure range ($p/p_0 < 0.01$), which suggested the presence of micropores with an average pore size between 0.49 and 0.66 nm. BET surface values showed that an increase in cationic dopant content led to an increase in the BET area value (Table 3). This experimental fact suggested that Ag atoms entered the framework of OMS–2, making the surface areas larger, whereas pore size distribution became sharper.

Table 3. Textural properties (N_2, 77K) of K–OMS–2 and [Ag]–K–OMS–2 materials.

Sample	Incorporated Ag Content (% wt.)	BET Surface Value (m^2/g)
1 [a]	0	76.9
2	0.1	79.1
3	0.5	79.7
4	1.5	81.2
5	2.0	81.8

[a] Undoped material K–OMS–2. Data were extracted from [153,154].

Nonetheless, since according to the geometric parameters of Ag^+, this replacement should theoretically take place even more easily in the tunnels, the new material was called Ag-hollandite (with general formula $Ag_{1.8}Mn_8O_{16}$).

Interestingly, [Ag]–K–OMS–2 was slightly different from the original cryptomelane. That is, silver cations did not occupy the center of the cages formed by MnO_6 octahedra units, but they were placed on the common face sites, which are coordinated with four oxygen anions, as could be elucidated by XRPD and electronic microscopy techniques. Indeed, the modification of the structure could be confirmed by XRPD, which showed changes with respect to the cryptomelane structure, as it can be seen in some examples in the literature [164–167] adjusting to a tetragonal structure, $Ag_{1.8}Mn_8O_{16}$ (ICDD # 01-077-1987).

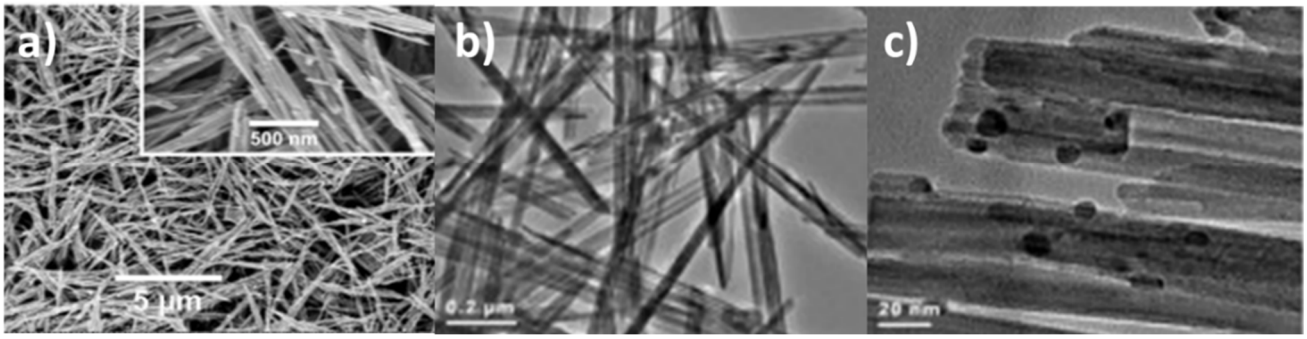

Figure 9. FESEM micrograph of [Ag]-OMS-2 catalyst (**a**), TEM and HR-TEM images showing the morphology of short nanofibers (**b**) and low magnification image showing the morphology of short nanofibers with Ag nanoparticles (**c**). Images have been extracted from [164].

Studies about the mobility of oxygen species were performed by means of temperature programmed techniques such as TPR and TPD experiments. All these techniques confirmed that the incorporation of Ag species into the framework improved the mobility of oxygen species, having a strong impact in catalytic reactions (see Section 3.2). This could be explained by means of a synergistic effect between Ag, both located in tunnels and at the level of framework, and the active centers of manganese oxide [153].

3.1.2. [Ce]–K–OMS–2

Ce ions can be incorporated into OMS–2 tunnels to replace K^+, but can be situated into the OMS–2 framework via isomorphic substitution starting from a precursor salt, i.e., $Ce(NO_3)_3{\cdot}6H_2O$, through a reflux method [106,168]. Indeed, depending on the amount of Ce incorporated, diverse structural changes could be detected by XRPD diffraction as well as by electron microscopy.

For example, an increase of crystal size took place after Ce incorporation, due to an expansion of the cell parameters as well as a slight aggregation of K–OMS–2 nanorods and a decrease of lattice fringes [155,156,169,170].

Similarly, as previously described for [Ag]–K–OMS–2, the incorporation of Ce as a dopant cation into the structure enhanced the surface area values [155,156,169].

NH_3-TPD was used in this case to evaluate the acid/base strength of the as-prepared materials. In this case, it was observed that the introduction of Ce increased the amount of strong acid sites over OMS catalysts. This was correlated with the NH_3 desorption area data (Table 4) calculated from [156].

Table 4. Acidic properties of Ce-doped K–OMS–2 ([Ce]–K–OMS–2) and undoped K–OMS–2. Data were extracted and adapted from [156].

Sample	Desorption Temperature (°C)			Peak Area (a.u.)			
	Peak I	Peak II	Peak III	Peak I	Peak II	Peak III	Total
K–OMS–2	108	492	581	302	422	448	1172
[Ce]–K–OMS–2	132	340	650	305	903	723	1931

According to the literature, peaks attributed to the weak acid sites appeared at ca. 110–115 °C; meanwhile, the desorption peaks at ca. 200–550 °C were assigned to strong acid sites [171]. Interestingly, after Ce-doping, all the peaks shifted to higher temperatures, indicating a stronger acidic behavior [156]. The total calculated area confirmed this trend (Table 4).

In parallel, FT-IR spectra of the materials could assess the local environment surrounding the structural Mn-O bonds. Effectively, variations in the FT-IR spectra indicated that Ce had been incorporated into the framework of K–OMS–2, resulting in the appearance of new structure vibrations, i.e., 582, 467 and 714 cm^{-1} [170].

Besides, additional studies showed that the reducibility of K–OMS–2 did not vary after the incorporation of Ce at the structural level because both TPR profiles were very similar [169,172].

Regarding XPS studies, they showed that the incorporation of Ce as a cationic dopant involved a higher concentration, ca. 10%, of lattice oxygen with respect to the undoped material K–OMS–2, and this experimental fact was also accompanied by a rearrangement of the manganese species (+3, +4 and +2) [156].

It is interesting to note that this material could also be used merely as a support, so that other oxides or metals could be deposited on the surface. For example, it is important to highlight the case of [Ce]–K–OMS–2 [173] doped with Au nanoparticles (AuNPs) [174], for which an increase in the amount of Ce (>6% wt. Ce) caused part of the Ce to be deposited on the structure and part on the surface, as was confirmed by electron microscopy (Figure 10) and XRDP [174].

In this case, the cooperation between AuNPs (smaller than 3 nm), CeO_2 species and the manganese oxide framework afforded unique properties to the system, improving its catalytic behavior in the CO oxidation reaction. In conclusion, the incorporation of cerium had an influence at two levels: (i) increased the number of defect sites, which had the ability to interact with gold nanoparticles and stabilize them, and (ii) increased the amount of extra-framework CeO_2 nanoparticles, which improved the charge transfer between Au and cryptomelane.

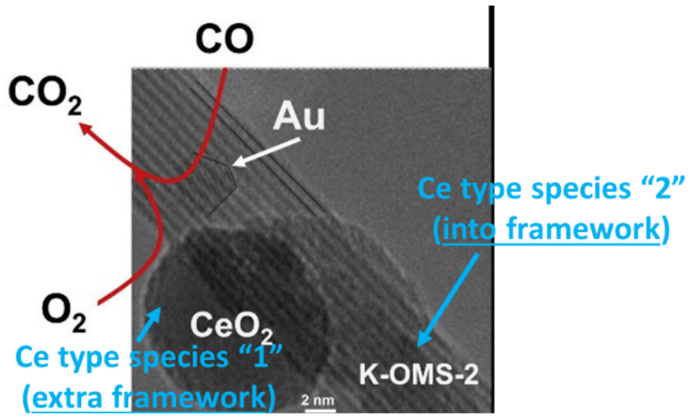

Figure 10. HR-TEM micrograph of Au supported on [Ce]–K–OMS–2. In the image, different types of Ce species are indicated (blue color). Besides, the role of each chemical species is indicated for the CO oxidation reaction. The image has been extracted and modified from [174].

3.1.3. [Ru]–K–OMS–2

Catalytic processes involving ruthenium had already been extensively studied during recent years [175–179].

For this reason, it seemed an ideal cation to be incorporated into the structure of K–OMS–2 in order to obtain a material with attractive properties. In this context, [Ru]–K–OMS–2 was obtained through a reflux method [108,133] starting from manganese precursor salts combined with $RuCl_3 \times H_2O$.

X-ray powder diffractograms (XRDP) showed that the ruthenium incorporation (2% by weight of ruthenium) did not induce obvious changes in the diffractogram pattern, albeit from refining XRPD data, a slight expansion of cell parameters could be clearly confirmed [108]. The presence of ruthenium into the structure was confirmed by combining analytical and vibrational techniques, such as ICP, UV-Vis, FT-IR and Raman spectroscopies, X-ray diffraction, electron microscopy (HR-TEM and SEM) and X-ray photoelectron spectroscopy [108].

In this regard, it is important to remark that the amount of Ru incorporated at the structural level in K–OMS–2 did not exceed 4.5% by weight [133], which is a significantly lower amount than that obtained for other smaller cations incorporated in the network (i.e., Co, Cu and Ni) [160,162,180]. As an example, the amount of Fe that can be incorporated in K–OMS–2 oxide ([Fe]–K–OMS–2) can reach up to 6% wt. of Fe [146].

At this point, it is important to note that one of the most prominent aspects of this material is the reducibility, a property that is closely associated to the weakening of the Mn-O bond [108,133]. In this context, it was observed that this weakening effect increased as the Ru content increased (Figure 11).

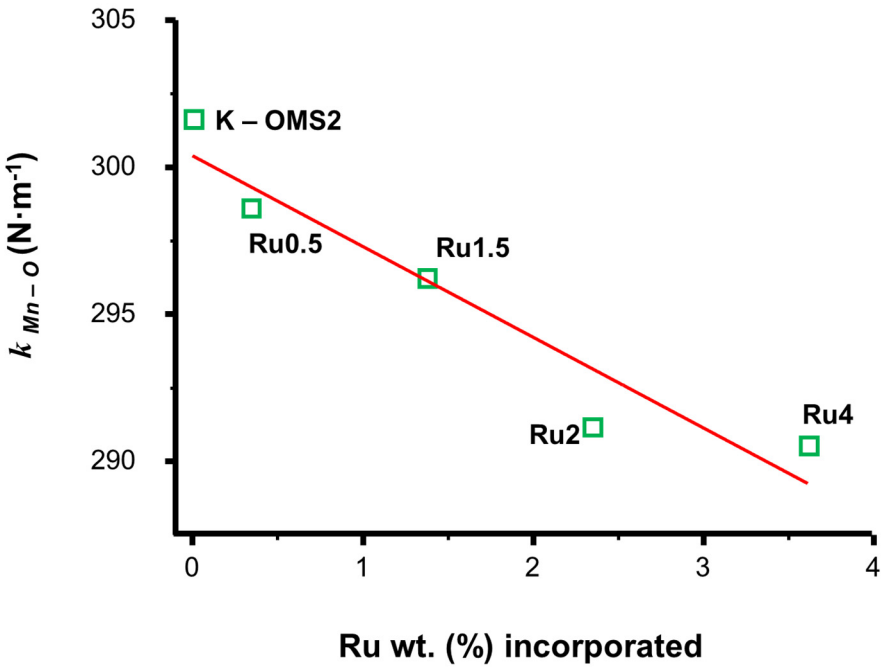

Figure 11. Graphic representation of the Mn-O strength (N·m^{-1}) versus the amount of ruthenium incorporated in the structure: Ru0.5 (0.5% wt.), Ru1.5 (1.5% wt.), Ru2 (2.0% wt.) and Ru4 (4.0% wt.). Extracted from [133].

Effectively, the results included in Figure 11 show that the increasing incorporation of Ru into the oxide K–OMS–2 causes a linear decrease in the Mn-O bond strength, a fact that becomes evident by the gradual decrease of the force constant value k_{Mn-O} (N·m^{-1}). This parameter that provides semi-quantitative type information from the Hook's law gave the lowest k_{Mn-O} (N·m^{-1}) value for the highest Ru content material [Ru(4%)]–K–OMS–2. This result is highly important because according to this, [Ru(4%)]–K–OMS–2

might be predicted as more reactive than any other oxide with lower Ru content during its performance as a catalyst, particularly in reactions that follow a Mars–van Krevelen mechanism (i.e., oxidations).

In this respect, one important consequence of this aspect could be the direct impact on reducibility, a property that can be measured by H_2-TPR (temperature programmed reduction) (Figure 12).

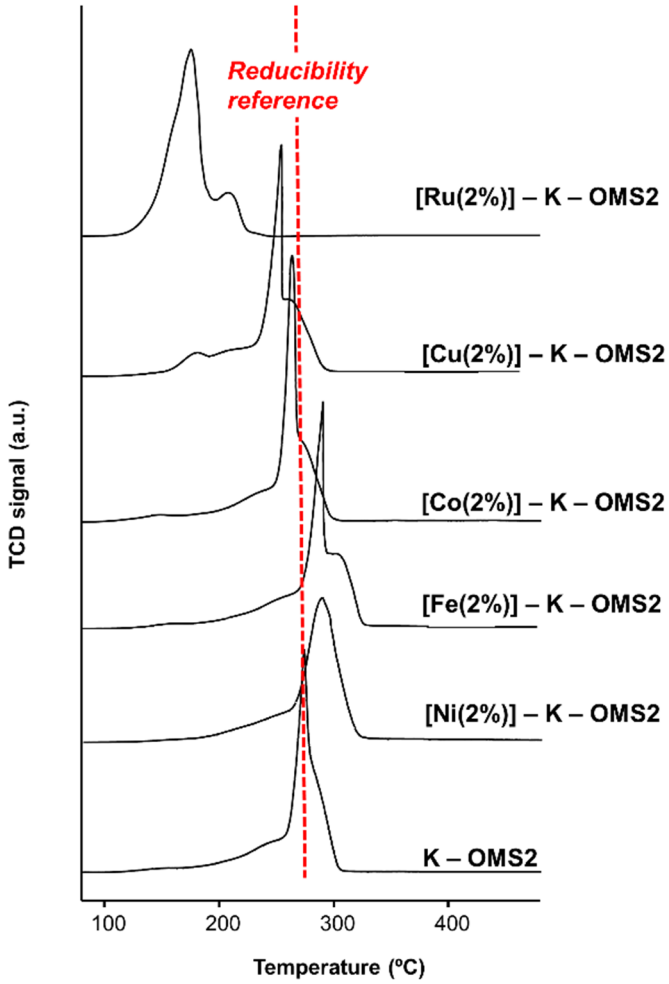

Figure 12. H_2-TPR profiles for [M]–K–OMS–2 materials and undoped K–OMS–2. Extracted and adapted from [133].

Indeed, Figure 12 shows the impressive effect that Ru has on the reducibility of K–OMS–2 with respect to a series of earth abundant metal cations assayed (i.e., Co, Ni, Cu and Fe). This impact has been attributed to a greater difference in size and properties of Ru versus Mn, with respect to more similar cations [108,133]

This feature should have an impact on the catalytic applications, as it will be shown in Section 3.2.2.

3.1.4. [Ti]–K–OMS–2

Ti^{4+} species have also been successfully incorporated into the framework of K–OMS–2 through a reflux method from the respective precursor salts [157]. In addition, since the ionic radius of Ti^{4+} (0.61 Å) is greater than that of Mn^{4+} (0.53 Å), an expansion of the cell volume should a priori be expected in case isomorphic substitution occurs [181]. In this regard, the cell volume expansion estimated for [Ti]–K–OMS–2, with a Ti/Mn ratio ranging from 0.18 to 0.43, was ca. 2%. In this case, all Ti species were exclusively located in the framework [157]. With higher Ti/Mn ratios (e.g., 0.5), the K–OMS–2 framework could not

hold all the titanium species, and they began to be deposited in extra framework positions. It is interesting to note that the surface areas of K–OMS–2 and [Ti]–K–OMS–2 were similar in both cases [157,182].

Nonetheless, interestingly, it appears that the impact that Ti-doped K–OMS–2 oxide has had in catalysis is lower than other metal-doped cryptomelane structures [182], in view of the low number of catalytic applications reported for this material (i.e., oxidation of styrene).

In this case, different techniques, such as XRPD, photoluminescence, surface area, etc., allowed to deduce the location of cationic species, whereas more powerful techniques such as electron microscopy with high resolution at the atomic level confirmed with great precision its location at the structural level (Figure 8) [144].

3.1.5. Doping with High-Valence Cations: [Mo]–K–OMS–2, [W]–K–OMS–2 and [V]–K–OMS–2

In principle, it is foreseeable that the isomorphic doping with high-valence cations (i.e., Mo^{6+}) would take place preferably at the structural level and not in the tunnels, accounting for the charge restrictions that must be inside the tunnels in order to keep the original structure intact [158]. In this line, a change from symmetry tetragonal (a "distorted" symmetry) to monoclinic could be observed after Mo^{6+} doping [158].

In this case, the isomorphic substitution leading to the formula $K_xMo^{6+}{}_{2y}\square^o{}_y Mn^{4+}{}_{1-x-3y}Mn^{3+}{}_xO_2$ went through the following equations, according to the authors of [150,158], where $\square^o$ indicates a required octahedral vacancy in the framework to balance the charge:

$$^{VI}Mo^{6+} + {}^{VI}\square^o \leftrightarrows 2\,{}^{VI}Mn^{3+}$$

$$2\,{}^{VI}Mo^{6+} + {}^{VI}\square^o \leftrightarrows 3\,{}^{VI}Mn^{4+}$$

In this case, the reported trend could also be envisaged in the XRP diffractograms by means of lattice and interplanar distance measurements, along with electron microscopy images and selected area electron diffraction (SAED) patterns, which unambiguously showed this change (Figure 13) [183].

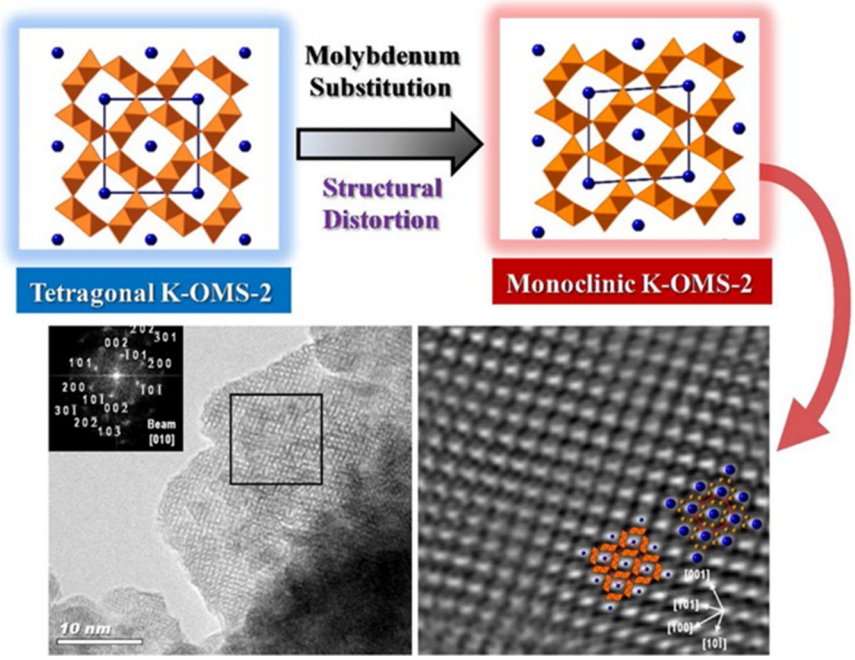

Figure 13. HR-TEM images showing the structural distortion of the original tetragonal K–OMS–2 structure due to the molybdenum substitution. On top, a brief scheme showing this transformation. Image extracted from [151].

Regarding the substitution with W, Table 5 shows the cell parameters obtained from Rietveld refinement obtained for [W]–K–OMS–2 materials with different W contents.

Table 5. Cell parameters obtained from Rietveld refinement of undoped (K–OMS–2) and [W]–K–OMS–2-doped materials. Data extracted from [151].

	K–OMS–2	[W(1.33%)]–K–OMS–2	[W(2%)]–K–OMS–2
a (Å), *b* (Å)	9.815	9.804	9.816
c (Å)	2.847	2.852	2.855
cell volume (Å^3)	274.3	274.1	275.1

Table 5 shows that there are slight differences in the lattice parameters for W-doped K–OMS–2 (1.33 and 2 mol% W) and those for the K–OMS–2 sample (taken as a reference). As discussed above [108], a low concentration of doping cation of a similar crystal radii, such as $^{VI}W^{6+}$, $^{VI}W^{4+}$, $^{VI}Mn^{4+}$ and $^{VI}Mn^{3+}$ (high spin and low spin), did not lead to significant structural differences between the undoped and W-doped structures [151]. Indeed, 1.33 mol% W caused a slight shrinkage of the unit cell, according to the *a* and *b* axes values. However, despite the fact that there were no significant differences in cell parameters of [W]–K–OMS–2 after W-doping, the modifications of the electronic environment were high enough to modulate properties related to conductivity for different applications [151].

Other useful information that could be obtained from the diffractograms has to do with the relative intensity of peaks and their positions. For the particular case of Mo, it has been reported [158] that the incorporation of large amounts of Mo into the structure (from Mo/Mn ratio $\geq$ 0.2) can lead to a broadening of the peaks and the collapse of the structure or amorphization. This trend is common for other high-valence species, i.e., V^{5+} and W^{6+} incorporated into the K–OMS–2 structure [151,158,160]. In this regard, it is important to keep in mind that there is a strong relationship between the valence of doping cations and the stability of K–OMS–2, which will be critical for keeping the electroneutrality of the system [158].

As informative data, amorphization processes are often accompanied by an increase of surface area, a shortening of the length/width ratio of nanorods and changes in the thermal stability of the materials [158].

Interestingly, spectroscopic Raman studies showed two main bands, at 578 and 640 cm^{-1}, that were related to Mn-O vibrations of the MnO_6 units [150]. In this case, the presence of these two bands confirmed that the framework local units were unchanged, so the tetragonal structure (space group *I*4/m) remained. Then, a progressive increase of the Mo content into the framework shifted the spectrum bands to higher wavelengths (blue-shift). When this increase was high enough, bands tended to disappear due to changes of the symmetry of the unit cell. Occasionally, bands related to MoO_x species could also be detected under these extremely severe conditions.

Another high-valence cation that can be incorporated into the framework is vanadium. There is a minimal difference in size (*ca.* 1 pm) between Mn^{4+} and V^{5+}, and this explains that the basal spacing of [V]–K–OMS–2 did not change with the incorporation of increasing amounts of vanadium [160]. However, quantitative analysis (i.e., EDX or ICP) showed that there is a limit to the amount of V incorporated into the framework (Figure 14).

Indeed, for those samples containing up to 8–10% V (blue line in Figure 14), a good correlation between the experimental vanadium content of the solid (determined by EDX) and the initial vanadium content of the reaction mixture could be found. However, a progressive deviation from the initial composition took place above this range with increasing vanadium concentration [160]. Meanwhile, the incorporation of vanadium species tended to rearrange the manganese framework species (Mn^{2+}, Mn^{3+} and Mn^{4+}), as confirmed by XPS [159].

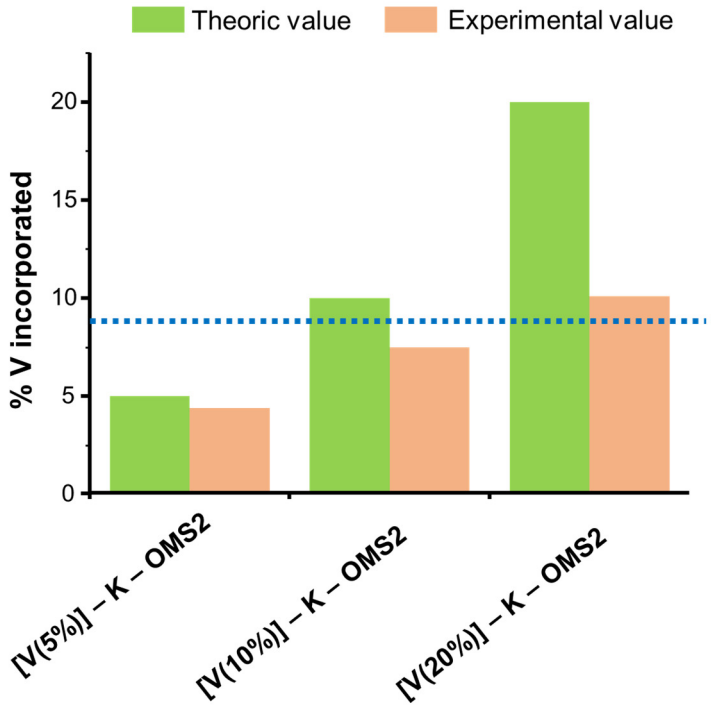

Figure 14. Comparison between the expected % wt. V incorporated and the experimental values obtained by EDX. The dotted blue line indicates the point from which a deviation between the expected and experimental values is observed. Data were extracted from [160].

Raman spectroscopy confirmed the formation of extra framework VO_x species with a high V content (greater than 10% wt.) through detection of the typical V=O vibration (range 970–1030 cm^{-1}) [160].

Finally, a new type of [V]–K–OMS–2 was synthesized consisting of a mesoporous K–OMS–2 system [184]. Mesoporous V-doped K–OMS–2 was synthesized by transforming amorphous V-doped mesoporous Mn_2O_3 under mild acidic conditions. Changes in morphology as well as an appreciable decrease in crystallinity were confirmed by electron microscopy upon increasing the percentage of V doping, as was described for other related doped materials. XPS results showed that the manganese was present as Mn^{2+}, Mn^{3+} and Mn^{4+}, whereas vanadium was present as V^{4+} in [V]–K–OMS–2 samples.

This material has shown interesting and promising results in hydrogen evolution reactions (HER) [184].

3.1.6. [Nb]–K–OMS–2

More recently, the replacement of Mn by relatively larger cations such as Nb in the framework of the octahedral molecular sieve K–OMS–2 was reported. In this case, up to 31 mol% (or even 43% wt.) were incorporated into the network. Above this content, the cryptomelane structure collapsed and an amorphous phase of Nb_2O_5 started to form [162].

Higher contents of Nb in the structure favored sintering processes that indeed took place at lower temperatures as a function of the Nb content.

According to XPS data, Nb was incorporated as Nb(V) species. Interestingly, TEM, STEM and HAADF imaging of Nb-doped K–OMS–2 materials showed retention of rod-like morphologies with subtle changes in *d* spacings and length/width ratios.

Indeed, the cryptomelane rod-type morphology of K–OMS–2 was maintained, even up to a 31% substitution. At higher Nb loadings, amorphous solids were obtained. Moreover, textural properties suggested that after replacement with Nb, the OMS–2 rods became less susceptible to particle growth and sintering took place more easily upon heating treatment (as compared to original K–OMS–2).

3.1.7. [In]–K–OMS–2

Indium tin oxide (ITO) and other indium-doped materials are of great interest as electrodes and sensors [185–187]. For this reason, a novel material based on the introduction of In species into the mixed-valent manganese framework (K–OMS–2) had a potential interest in this field. The synthesis of the indium-doped K–OMS–2 material, [In]–K–OMS–2, involved a hydrothermal treatment [188]. XRPD diffractograms showed that there were no changes in the original cryptomelane structure up to an In/Mn ratio of 0.019. As it was shown for [V]–K–OMS–2 oxide (Section 3.1.5), EDX analysis suggested that there is limited solubility of indium oxide in K–OMS–2 [188]. Besides, a potentiometric titration method measured the average oxidation state of the doped and undoped materials. Interestingly, the incorporation of In up to a limit of 1/5 (In/Mn) enhanced the average oxidation state (AOS) ca. 3% with respect to AOS of K–OMS–2. For all the cases [188], no segregated pure In phases were detected neither by XRD, Raman spectroscopy nor electronic microscopy (Section 3.1.8, Figure 15a).

3.1.8. [Zn]–K–OMS–2 and [Zr]–K–OMS–2

Both materials were synthesized through a reflux method, starting from manganese and the respective Zn or Zr precursor salts, i.e., $Zn(CH_3COO)_2{\cdot}2H_2O$ and $Zr(NO_3)_4{\cdot}5H_2O$ [189]. No segregated phases could be detected for both doped materials when Zn and Zr contents were moderate (ranging from 0.5 to 8 mol%), so the original cryptomelane structure remained unchanged under these experimental conditions. As in previous cases, this fact was interpreted in the sense that cationic dopants were well-dispersed in the K–OMS–2 structure.

Interestingly, the surface area of pure K–OMS–2 increased after doping with Zn and Zr (*ca.* 34% and 254%, respectively). Moreover, the addition of these cations resulted in the formation of oxygen vacant defects (OVDs), leading to a lower pore size and lower total pore volume, whereas doping with Zn and Zr had little impact on the AOS values, provided the AOS of manganese ranged in a narrow window of ca. 3.9–4.0. Similarly, changes in the morphology of nanorods after doping processes were in line with previously described materials, in the sense that they remained unchanged, i.e., [Zn]–K–OMS–2 (Figure 15b). On the contrary, [Zr]–K–OMS–2 experienced morphological changes at higher metal contents (Figure 15c).

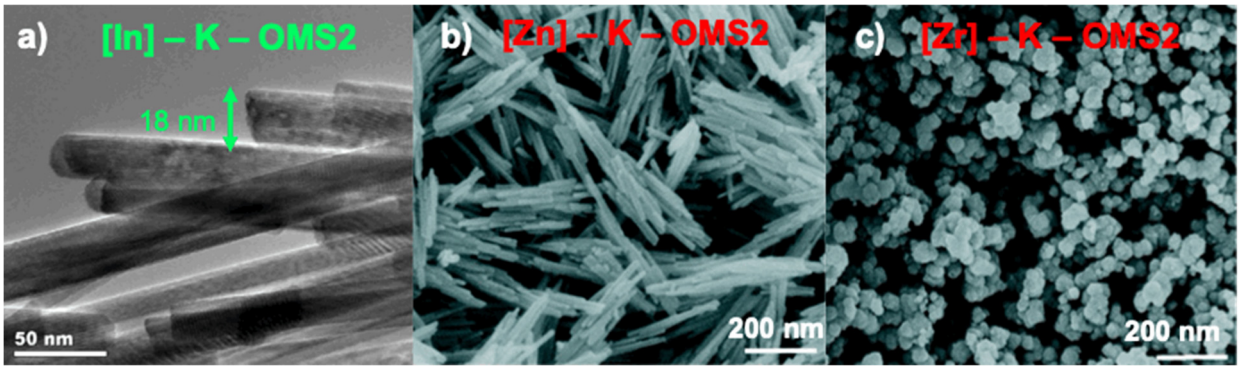

Figure 15. TEM image of [In]–K–OMS–2 (In/Mn = 1/5) (**a**), and FESEM images for [Zn]–K–OMS–2 (0.49% mol Zn) (**b**) and [Zr]–K–OMS–2 (7.50% mol Zr) (**c**). Images have been extracted and later adapted from references [188,189].

Finally, the H_2-TPR profiles for both materials [189] showed that the incorporation of both cations improved the reducibility of the oxide, because the reduction processes took place at lower temperatures with respect to K–OMS–2, although the respective reduction temperatures were still higher than that reported for [Ru]–K–OMS–2 (Section 3.1.3).

In the next section, we will describe catalytic applications for some of the above-described doped materials of [M]–K–OMS–2, and in some cases, when appropriate, a comparison between their performance will be carried out.

3.2. Catalytic Applications

3.2.1. [Ce]–K–OMS–2 as a Catalyst for General Pollutant Control Processes

Several studies have reported the O_3 decomposition as well as catalytic total oxidation (CTO) of tricholoroethylene (TCE) in the presence of [M]–K–OMS–2 as a catalyst [100]. In this regard, it is important to note that the presence of O_3 at high concentrations can induce health problems to humans (neurological diseases, reduced immune system function, etc.). For this reason, the conversion of environmental ozone is very important.

In this case, it seems that the doping cations enhanced the oxidative processes of different plasma-generated hazardous gaseous species (i.e., phosgene, trichloroacetaldehyde and dichloroacetylchloride). These processes have been described in the following equations [100,190]:

$$Cl_2CO + 5/3\ O_3 \rightarrow CO_2 + Cl_2 + 2\ O_2$$

$$C_2Cl_3OH + (10/3)\ O_3 \rightarrow 2\ CO_2 + Cl_2 + HCl + 7/2\ O_2$$

$$C_2Cl_3H + 4\ O_3 \rightarrow 2\ CO_2 + Cl_2 + HCl + 4\ O_2$$

Degradation of ozone (O_3) has also been studied using other [M]–K–OMS–2 materials [106]. In this sense, ozone was decomposed under real conditions, in the presence of water molecules [106,191]. From these experiments, it could be deduced that water molecules had a severe influence on the catalytic performance because they competed with ozone for adsorption on the oxide surface, leading to a decrease in catalytic activity. With the aim to carry out this study, several doped [M]–K–OMS–2 oxides with abundant metal cations were synthesized (M: [Co], [Ce] and [Fe]) [106] through a hydrothermal method from the respective precursor salts, cerium(III), cobalt(II) and iron(III) nitrates respectively, just for comparison [106].

Characterization techniques (i.e., XRPD) suggested that all these doped oxides were obtained as pure phases, and the tunnel structure remained unchanged [106]. However, the position of metallic species seemed to be slightly different in each case. On the basis of the results summarized in Table 6, it is possible to propose different substitution patterns. In principle, the K/(Mn + M + K) values for [Fe]–K–OMS–2 and [Co]–K–OMS–2 (6.40% and 6.31%, respectively) were similar to those of K–OMS–2 (6.37%). It indicates that relative quantity does not change, so this fact suggested that the metal was incorporated into the structure. In other words, Co^{3+} and Fe^{3+} species compete effectively with Mn^{3+} ions for a place in the structure.

In the case of [Ce]–K–OMS–2, it showed a decrease of both K/(Mn + M + K) and Mn/(Mn + M + K) ratios with respect to the K–OMS–2 values. This suggested that the substitution of both types of Mn valent ions in the framework as well as K^+ in the tunnel sites of OMS–2 took place. This is also supported by the fact that the Mn/Mn + M + K ratios in [Ce]–OMS–2 materials were higher than those in [Co]–OMS–2 materials [106].

The replacement of K^+ by Ce^{4+}/Ce^{3+} cations may lead to a distortion of the crystal, provided that Ce cations have a smaller radius than K^+ (up to *ca*. 50% smaller radius size). This distortion has been reported in the literature even for other cases [106,156] through SEM microscopy. Nevertheless, the distortion found for [Fe]–K–OMS–2 and [Co]–K–OMS–2 was less marked given that the content in the framework was not very high [158,192].

XANES analysis confirmed that cobalt and iron species were replacing Mn^{3+} cations in the cryptomelane framework, whereas Ce^{4+} was mainly replacing K^+ in the tunnels and part of Mn^{4+} species in the cryptomelane framework [106]. These observations were very important in order to explain the catalytic results summarized in Figure 16.

Table 6. Properties and characteristics of [M]–K–OMS–2 and K–OMS–2 oxides used in the degradation of ozone. Data were extracted from [106].

Catalysts	K/Mn + Metal + K (%) [a]	Mn/Mn + Metal + K (%) [a]	Metallic Dopant Species (% abundance) [b]	Surface Area (m^2/g) [c]
K–OMS–2	6.37	93.6	-	137
[Ce]–K–OMS–2	4.82	86.7	Ce^{3+} (30%), Ce^{4+} (70%)	200
[Co]–K–OMS–2	6.40	85.1	Co^{3+} (95%) [d], Co^{2+}(5%) [e]	115
[Fe]–K–OMS–2	6.31	83.6	Fe^{2+} (36%) [d], Fe^{3+}(64%) [e],	52

[a] ICP values, [b] XPS values, [c] N_2 adsorption (77K), [d] Octahedral position, [e] Tetrahedral position.

At this point, it was proposed that the Mn^{3+} content seemed to play a key role during ozone decomposition. The degradation process of ozone catalyzed by noble metal and transition metal oxide catalysts is based on three steps [193]:

1. An O_3 molecule is adsorbed on the surface of the catalyst, and then dissociates into an oxygen molecule and an atomic oxygen species.
2. The remaining atomic oxygen species react with another ozone molecule to form an adsorbed peroxide species (O_2^{2-}) or superoxide (O_2^-) and an oxygen molecule.
3. Adsorbed O_2^{2-} or O_2^- decompose into oxygen molecules and desorb from the active site of catalysts

In accordance with this, it was proposed that abundant Mn^{3+} species (surface oxygen vacancies) on the surface may enhance, they act as active species, the ozone decomposition process (first and second step), as it follows from the equations [106]:

$$O_3 + [Mn^{3+}] \rightarrow O_2 + O^-_{ads}[Mn^{4+}]$$

$$O_3 + O^-_{ads}[Mn^{4+}] \rightarrow 2O_2 + [Mn^{3+}]$$

Meanwhile, to explain the good results with [Ce]–K–OMS–2, it was suggested that the existence of oxygen vacancies related to Ce^{4+} in the framework could enhance the oxygenated species' mobility.

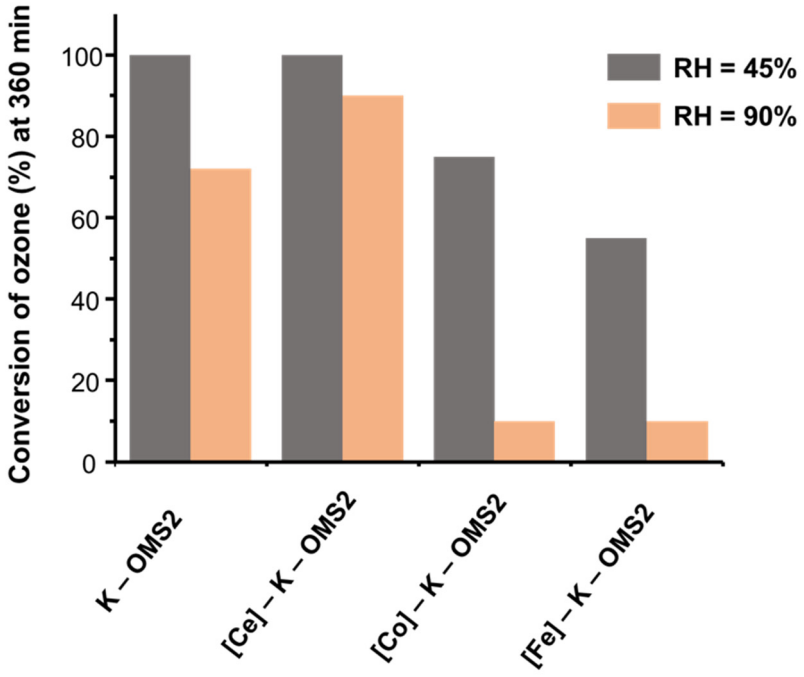

Figure 16. Conversion of ozone at 360 min with isomorphic Ce-, Co- and Fe-doped, and undoped (K–OMS–2) catalysts at different relative humidity (RH) values. Data extracted from [106].

In summary, it was proposed that the material with the highest Mn^{3+} content ([Ce]–K–OMS–2) showed the best catalytic results, obtaining high conversion values (*ca.* 90%) at high values of humidity (relative humidity = 90%). In this case, it seemed that the surface area values (Table 5) did not have a decisive impact on catalytic activity nor the metal doping as it did not detect a clear trend.

Interestingly some other reactions required materials with a higher ratio of manganese replacement. For example, it was observed that [Co]–K–OMS–2, [Cu]–K–OMS–2 and [Fe]–K–OMS–2 were active for acetaldehyde degradation [155]. However, [Co]–K–OMS–2 supported on alumina (Al_2O_3) showed the best catalytic activity. This was attributed to a higher level of Mn replacement on the first catalyst layers and to a more improved redox capacity, surface area and oxygen mobility (among the most influencing parameters) with respect to other isomorphic materials. According to the proposed mechanism [155], the redox pairs Mn^{n+}/Mn^{n+2} and $M^{n+}/M^{(n+2)+}$ plays an important role. This is the reason why [Co]–K–OMS–2 system, due to having a greater proportion of these active species, has a higher activity [155].

On the other hand, it is worth mentioning a novel study where a correlation between catalytic activity and location of the doping cation was shown. In particular, the activity of Fe-doped materials during degradation of pollutants (i.e., phosgene, trichloroacetaldehyde and dichloroacetylchloride) will depend on Fe location (at the structural level, [Fe]-K–OMS–2, or on the surface, Fe/K–OMS–2) [100].

The most prominent difference between them was the reducibility, since the onset of reduction temperature decreased as follows: K–OMS–2 > Fe/K–OMS–2 > [Fe]–K–OMS–2. This same trend has also been observed for Ru-doped cryptomelane materials [108] (see Section 3.2.2).

This improved oxygen ability observed for [Fe]–K–OMS–2 could be related to oxygen vacancy defects, which would promote the degradation of VOC and reaction intermediates [100]. In this case, it was suggested that the higher reducibility of surface Mn^{4+} species and the existence of a collaborative effect between Mn and Fe species could facilitate the decomposition of O_3 to obtain active oxygen atoms that improve the mobility of surface oxygen of the catalyst [100]. Similar trends were observed for Fe-doped cryptomelane materials used in the oxidative dehydrogenation of ethanol [194].

3.2.2. [Ru]–K–OMS–2 as a Catalyst for Fine Chemicals

Isomorphic ruthenium-doped cryptomelane material, [Ru]–K–OMS–2, has recently been synthesized [108]. The presence of ruthenium in the structure was confirmed by means of analytical and vibrational techniques, such as ICP, UV-Vis, FT-IR and Raman spectroscopies, X-ray diffraction, electron microscopy (HR-TEM and SEM) and X-ray photoelectron spectroscopy [108]. Moreover, Rietveld refinement of the XRP diffractograms showed an expansion of the cell parameters which were compatible with an isomorphic ruthenium substitution [108].

One of the most important consequences of the isomorphic substitution is the weakening of the Mn-O bond, which was evidenced by means of semi-quantitative calculations from Raman vibration modes. Interestingly, doping with ruthenium showed a remarkable effect on the original reducibility of the K–OMS–2 [108,175] (see Section 3.1.3).

This had important implications in catalysis, especially for those reactions that follow a Mars–van Krevelen-type oxidation mechanism, such as the oxidation of alcohols to aldehydes. For this purpose, the benzyl alcohol to benzaldehyde transformation was chosen to evaluate the role of ruthenium in the framework, [Ru]–K–OMS–2, on the surface, RuO_x/K–OMS–2, and the original K–OMS–2 for comparison.

Figure 17a shows that the incorporation of ruthenium into the structure had a higher impact on the initial reaction rate (r_0) than other metal-doped materials (up to 4 times) [108]. This experimental fact could be explained by taking into account that the mobility of oxygen species improved after Ru-doping.

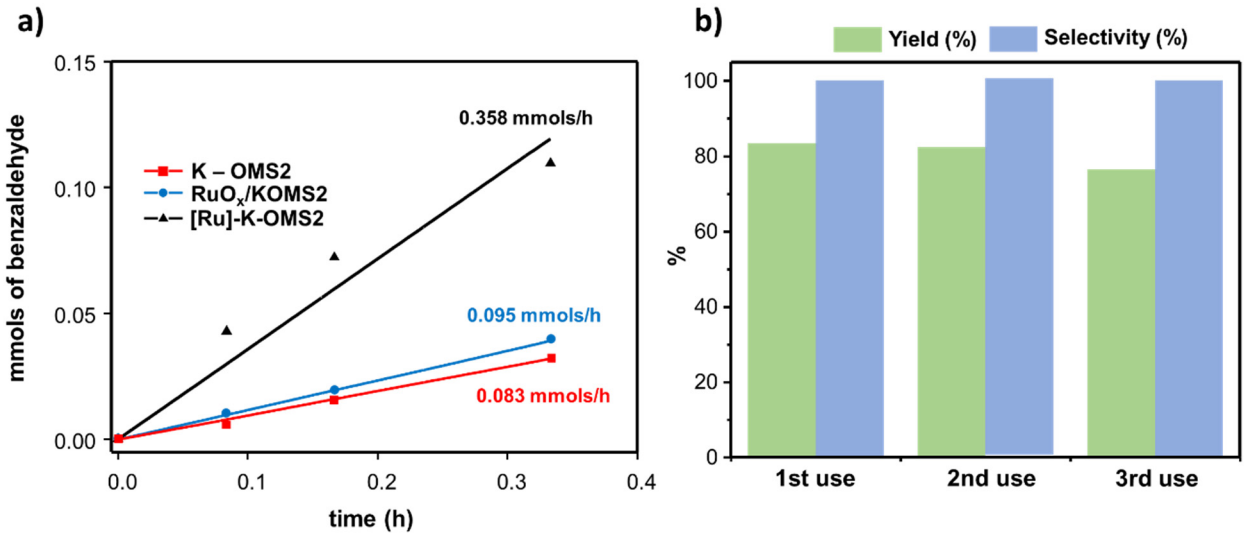

Figure 17. (**a**) Initial reaction rates (r_0) calculated from the respective tangent lines for each catalyst, and (**b**) studies on recovery and reuse of the [Ru]–K–OMS–2 catalyst. Experimental data for both graphics can be found in [108].

Mechanistic studies were carried out using the benzyl alcohol oxidation to benzaldehyde as a model reaction [129,195]. In this case, the organic substrate would be oxidized by Mn^{4+}, which would undergo a two-electron reduction from Mn^{4+} to Mn^{2+}. In a second step, Mn^{2+} would undergo a two-electron reoxidation [108,133], with the intervention of the cationic dopant, which means that Ru would assist in the two-electron reoxidation of Mn^{2+} species. Finally, Ru species would combine with molecular oxygen to close the catalytic cycle. Basically, the role of Ru would be restricted to re-oxidizing manganese reduced species to Mn^{3+} and Mn^{4+} and maintaining the neutrality of the structure.

In this reaction, the heterogeneity of the process was confirmed provided that [Ru]–K–OMS–2 could be recovered and reused up to three times without a significant loss of activity, selectivity and catalytic properties (Figure 17b). For achieving this, the catalyst was calcined (310 °C during 2 h) after use in order to remove the organic adsorbed species on the surface [34,151,152].

In addition to this and according to the recent literature [196,197], [Ru]–K–OMS–2 seems to also have promising applications in the field of electrocatalysis and energy storage.

3.2.3. [Ag]–, [Nb]–, [Mo]–, [V]–, [Cu]– and [Zn]–K–OMS–2 as Catalysts for CO Oxidation

This section will cover the use of [M]–K–OMS–2 as a catalyst to remove carbon monoxide (CO) gas through the low-temperature CO oxidation.

Given that CO is produced in human activities (i.e., industrial waste gases, exhaust gas from automobiles, etc.) and it is very harmful to humans and the environment, the catalytic oxidation of CO is part of some strategies in order to reduce emissions of this gas to the environment [164]. In this regard, the methodology of transforming CO is very promising due to its low cost and high efficiency. However, the fact that numerous catalysts involved in this procedure usually contain supported noble metals, such as: Pt, Pd, Rh, Ru, Au, Ag, etc. [198–202], makes the process rather expensive. For this reason, investigations have focused on developing useful catalysts based on earth-abundant metal cations or non-expensive metals.

In principle, it appears that CO catalytic oxidation follows a redox mechanism on the surface of metal oxide catalysts consisting of the lattice oxygen reacting with adsorbed CO. Then, molecular oxygen would fill the oxygen vacancies that remain. According to this mechanism, the key for improving the catalytic activity of OMS–2 is the promotion of the surface lattice oxygen reactivity [139,203]. For this reason, it seems that manganese octahedral molecular sieves could be excellent candidates for this reaction [153].

In this context, Table 7 includes the results of CO oxidation in the presence of a series of [M]–K–OMS–2 catalysts reported during the most recent years in order to compare their activity.

Table 7. List of recently doped K–OMS–2 catalysts applied in CO oxidation.

Dopant [M]	Material	Location of M [a]	Reference
Ag	[Ag]–K–OMS–2	F, T, S	[164,204,205]
Nb	[Nb]–K–OMS–2	F	[206]
Mo	[Mo]–K–OMS–2	F	[207]
V	[V]–K–OMS–2	F	[159]
Cu	[Cu]–K–OMS–2	F, S	[136,141]
Zn	[Zn]–K–OMS–2	F	[208]

[a] Location of the dopant cation: (F) framework, (T) tunnel and (S) surface. Each location is determined from the indicated references.

The list of materials included in Table 7 confirmed the effectiveness of metal doping in cryptomelane materials for the CO oxidation. These materials were obtained through a wide variety of synthesis methods that allowed to control the location of the cation so that the properties of materials could be adjusted ad hoc.

For example, it was shown that the presence of stable Ag^{o}/Ag^{+} species had a critical role in the activity of the catalyst [164]. In this sense, the superior performance observed for Ag/K–OMS–2 (doped at the surface level) and Ag/[Ag]–K–OMS–2 (doped both at the surface and structural level) after post-reduction treatment with respect to undoped K–OMS–2 was attributed to the presence of highly dispersed silver species and to the unique redox properties that arise from intimate metal–support interactions. These interactions will promote the Mars–van Krevelen mechanism [164].

In principle, this intrinsic relation between the doping species and the manganese framework seems to be highly relevant, because changes in the electronic local environment can induce interesting synergic effects that will be reflected in catalysis. This has been reported to also occur for Cu-doped systems, where such Cu species are located on the surface and/or in the framework [136,137,141,209].

The cases of [V]–K–OMS–2, [Nb]–K–OMS–2 and [Mo]–K–OMS–2 deserve a special mention. For all the reported cases, considerable amounts of cationic dopant could be incorporated into the framework, i.e., 5–15% wt. [159,206,207]. However, given that cations with a larger ionic radius than Cu and Ag can more easily induce a unit cell expansion, the respective doping processes should be carried out by carefully controlling the process in order to ensure that the local structures do not collapse.

Interestingly, one of the trends confirmed that water molecules adsorbed on the surface completely inhibited the catalytic activity for the undoped K–OMS–2 catalyst during the CO oxidation (Figure 16) [159], and therefore higher temperatures were needed to reach the same catalytic values under anhydrous conditions. However, the incorporation of metal species into the structure clearly improved the CO conversion with respect to undoped K–OMS–2 because water molecules had a less negative effect on catalytic activity for the case of [Nb]–K–OMS–2 (Figure 18).

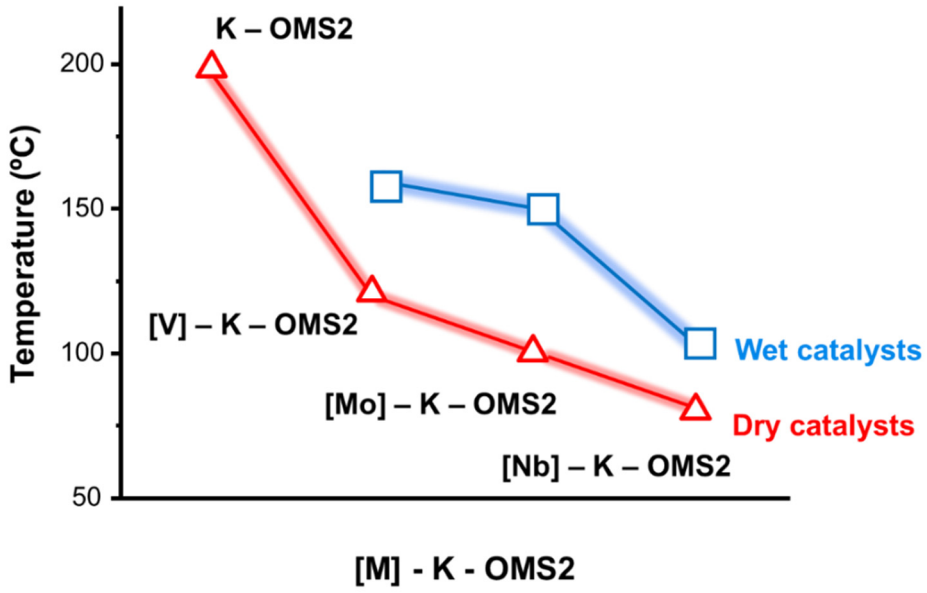

Figure 18. Relationship between metal doping [M: V, Mo and Nb] incorporated into the K–OMS–2 structure ([V(10%)]–K–OMS–2, [Mo(5%)]–K–OMS–2, [Nb(10%)]–K–OMS–2) and temperature needed to reach 50% CO conversion under wet and dry conditions, respectively. Data were extracted from [159,206,207] only for qualitative interpretation purposes.

Interestingly, the activity of [Zn]–K–OMS–2 seemed to be directly driven by the higher reducibility that K–OMS–2 showed when Zn(II) cations were incorporated into the structure, a feature that improved much more after UV-Vis-IR irradiation [208].

Finally, although it goes beyond the aim of this review, we must highlight the investigations [210] based on transition metal oxide nano-coatings on manganese oxide nanoarray monoliths, i.e., OMS–2@Co_3O_4 and OMS–2@TiO_2, which could also be used in the low-temperature CO oxidation. The activity of these materials seemed to be closely correlated to the amount of M^{n+} exposed on the surface, adsorbed oxygen species and oxygen mobility.

3.2.4. Other High-Impact Applications

It is necessary to highlight the role of isomorphic substituted materials, such as [W]–K–OMS–2, [V]–K–OMS–2, [Zr]–K–OMS, [Zn]–K–OMS–2, [Fe]–K–OMS–2 and [Mo]–K–OMS–2 during NH_3-SCR reaction [189], and the activity of [Nb]–K–OMS–2 in soot combustion reactions [161]. Besides, it is important to remark on the importance of [Fe]–K–OMS–2, [Co]–K–OMS–2 and [Ni]–K–OM2 in the oxygen-evolution reaction (OER) [211] as well as the role of [Nb]–K–OMS–2 in selective oxidation of methanol to dimethoxymethane and OER reactions [162] and the use of [Co]–K–OMS–2 as sorbents for the removal of H_2S [104].

4. Conclusions and Future Trends

This review discussed the metal isomorphic substitution of cryptomelane [M]–K–OMS–2 oxides that have appeared recently in the literature. In particular, we have addressed their syntheses on the basis of the replacement of manganese species in the framework by other transition metal cations with the proper size and coordination ability for this aim. This process, called isomorphic substitution, consists of the incorporation of different cations into the structure, a fact that will induce changes in the local environment and will give rise to new oxygen vacancies that will improve the catalytic ability for some reactions. In order to confirm the location of the cations after synthesis, we have stressed the importance of characterization techniques (even the more advanced ones if necessary for this purpose). In this regard, the proper combination of typical surface characterization techniques will

provide an unambiguous map to locate these new metal cations in the new material, which is a key point for catalytic activity.

In this regard, we have shown that [M]–K–OMS–2 oxides doped with Ag, Ce, Ru, Mo, V, Ti and Nb have interesting properties for being applied as catalysts in degradation of pollutants, CO oxidation reaction and synthesis of fine chemicals. The review has also shown that there is a constant and growing innovation of synthesis methods (i.e., processes, precursors, director agents, instrumentation) in order to obtain new [M]–K–OMS–2 materials with improved properties.

So far, cryptomelane [M]–K–OMS–2 oxides have been successfully applied in areas related to production and energy storage, such as manufacture of batteries, fuel cells and other devices, judging by the references on the subject. Nevertheless, their use as catalysts has attracted increasing attention in recent years (see Section 2.2) due to their high redox versatility. In particular, doping processes have occupied a prominent place in research due to the great variety of doping methods with different metal cations and the large number of catalytic applications that have been reported in the more recent literature.

No less important is the effort that has been made to correlate the catalytic activity to physical–chemical properties of [M]–K–OMS–2 oxides. Indeed, attempts have been made to rationalize the effects induced by the doping process in order to optimize the material properties and maximize the catalytic activity (see Section 2).

For this purpose, we must rely on characterization techniques in order to deeply investigate their properties. In this sense, advanced characterization techniques such as electron microscopy, synchrotron light sources, etc., as well as theoretical calculations will help to advance much faster, being key to expanding the list of catalytic applications of these materials in the near future.

Author Contributions: Conceptualization, M.J.S. and F.S.; writing—original draft preparation, F.S.; writing—review and editing, M.J.S.; supervision, M.J.S.; project administration, M.J.S.; funding acquisition, M.J.S. Both authors have read and agreed to the published version of the manuscript.

Funding: This research was funded by the Ministerio de Ciencia e Innovación (Gobierno de España) through the Severo Ochoa Program (SEV2016–0683) and Programa Estatal de Generación de Conocimiento (PGC2018–101247–B–00).

Acknowledgments: This work has been supported by Ministerio de Ciencia e Innovación through the Severo Ochoa Program (SEV 2016–0683) and Ministerio de Ciencia e Innovación, Programa Estatal de Generación de Conocimiento (PGC2018–101247–B–100). F.S. acknowledges the Spanish Government for Predoctoral FPI—Severo Ochoa scholarship (BES-2015-072719).

Conflicts of Interest: There are no conflict to declare.

References

1. Neculita, C.M.; Rosa, E. A review of the implications and challenges of manganese removal from mine drainage. *Chemosphere* **2019**, *214*, 491–510. [CrossRef]
2. Post, J.E. Manganese oxide minerals: Crystal structures and economic and environmental significance. *Proc. Natl. Acad. Sci. USA* **1999**, *96*, 3447–3454. [CrossRef]
3. Park, J.H.; Kim, B.-S.; Chon, C.-M. Characterization of iron and manganese minerals and their associated microbiota in different mine sites to reveal the potential interactions of microbiota with mineral formation. *Chemosphere* **2018**, *191*, 245–252. [CrossRef] [PubMed]
4. Costas, M. Z=25, manganeso, Mn. El metal del centro generador de O_2 en la fotosíntesis. *Anales de Química de la RSEQ* **2019**, *115*, 87.
5. Bertini, I.; Gray, H.; Stiefel, E.; Valentine, J. *Biological Inorganic Chemistry*; University Science Books: Sausalito, CA, USA, 2007.
6. Luo, C.; Tian, Z.; Yang, B.; Zhang, L.; Yan, S. Manganese dioxide/iron oxide/acid oxidized multi-walled carbon nanotube magnetic nanocomposite for enhanced hexavalent chromium removal. *Chem. Eng. J.* **2013**, *234*, 256–265. [CrossRef]
7. Wan, S.; Ding, W.; Wang, Y.; Wu, J.; Gu, Y.; He, F. Manganese oxide nanoparticles impregnated graphene oxide aggregates for cadmium and copper remediation. *Chem. Eng. J.* **2018**, *350*, 1135–1143. [CrossRef]
8. Wu, H.; Xu, X.; Shi, L.; Yin, Y.; Zhang, L.-C.; Wu, Z.; Duan, X.; Wang, S.; Sun, H. Manganese oxide integrated catalytic ceramic membrane for degradation of organic pollutants using sulfate radicals. *Water Res.* **2019**, *167*, 115110. [CrossRef]

9. Smirniotis, P.G.; Peña, D.A.; Uphade, B.S. Low-Temperature Selective Catalytic Reduction (SCR) of NO with NH3 by Using Mn, Cr, and Cu Oxides Supported on Hombikat TiO_2. *Angew. Chem. Int. Ed.* **2001**, *40*, 2479–2482. [CrossRef]
10. Dismukes, G.C.; Brimblecombe, R.; Felton, G.A.N.; Pryadun, R.S.; Sheats, J.E.; Spiccia, L.; Swiegers, G.F. Development of Bioinspired Mn4O4−Cubane Water Oxidation Catalysts: Lessons from Photosynthesis. *Acc. Chem. Res.* **2009**, *42*, 1935–1943. [CrossRef]
11. Kim, S.C.; Shim, W.G. Catalytic combustion of VOCs over a series of manganese oxide catalysts. *Appl. Catal. B Environ.* **2010**, *98*, 180–185. [CrossRef]
12. Qi, G.; Yang, R.T.; Chang, R. MnOx-CeO_2 mixed oxides prepared by co-precipitation for selective catalytic reduction of NO with NH3 at low temperatures. *Appl. Catal. B Environ.* **2004**, *51*, 93–106. [CrossRef]
13. Kamal, M.S.; Razzak, S.A.; Hossain, M.M. Catalytic oxidation of volatile organic compounds (VOCs)—A review. *Atmos. Environ.* **2016**, *140*, 117–134. [CrossRef]
14. Gorlin, Y.; Jaramillo, T.F. A Bifunctional Nonprecious Metal Catalyst for Oxygen Reduction and Water Oxidation. *J. Am. Chem. Soc.* **2010**, *132*, 13612–13614. [CrossRef] [PubMed]
15. Julien, C.M.; Mauger, A. Nanostructured MnO_2 as Electrode Materials for Energy Storage. *Nanomaterials* **2017**, *7*, 396. [CrossRef] [PubMed]
16. Wei, W.; Cui, X.; Chen, W.; Ivey, D.G. Manganese oxide-based materials as electrochemical supercapacitor electrodes. *Chem. Soc. Rev.* **2011**, *40*, 1697–1721. [CrossRef] [PubMed]
17. Wang, R.; Ma, Y.; Wang, H.; Key, J.; Brett, D.; Ji, S.; Yin, S.; Shen, P.K. A cost effective, highly porous, manganese oxide/carbon supercapacitor material with high rate capability. *J. Mater. Chem. A* **2016**, *4*, 5390–5394. [CrossRef]
18. Thackeray, M.M. Manganese oxides for lithium batteries. *Prog. Solid State Chem.* **1997**, *25*, 1–71. [CrossRef]
19. Liu, X.; Chen, C.; Zhao, Y.; Jia, B. A Review on the Synthesis of Manganese Oxide Nanomaterials and Their Applications on Lithium-Ion Batteries. *J. Nanomater.* **2013**, *2013*, 736375. [CrossRef]
20. Margreth, M.; Schlink, R.; Steinbach, A. Water Determination by Karl Fischer Titration. In *Pharmaceutical Sciences Encyclopedia: Drug Discovery, Development, and Manufacturing*; Wiley: Hoboken, NJ, USA, 2010. [CrossRef]
21. Carrillo, A.J.; Pizarro, P.; Coronado, J.M. Assessing Cr incorporation in Mn_2O_3/Mn_3O_4 redox materials for thermochemical heat storage applications. *J. Energy Storage* **2021**, *33*, 102028. [CrossRef]
22. Yang, G.; Xu, L.; Chao, Y.; Xu, J.; Sun, X.; Wu, Y.; Peng, R.; Liu, Z. Hollow MnO_2 as a tumor-microenvironment-responsive biodegradable nano-platform for combination therapy favoring antitumor immune responses. *Nat. Commun.* **2017**, *8*, 902. [CrossRef]
23. Wu, M.; Hou, P.; Dong, L.; Cai, L.; Chen, Z.; Zhao, M.; Li, J. Manganese dioxide nanosheets: From preparation to biomedical applications. *Int. J. Nanomed.* **2019**, *14*, 4781–4800. [CrossRef]
24. Kim, T.; Momin, E.; Choi, J.; Yuan, K.; Zaidi, H.; Kim, J.; Park, M.; Lee, N.; McMahon, M.T.; Quinones-Hinojosa, A.; et al. Mesoporous Silica-Coated Hollow Manganese Oxide Nanoparticles as Positive T1 Contrast Agents for Labeling and MRI Tracking of Adipose-Derived Mesenchymal Stem Cells. *J. Am. Chem. Soc.* **2011**, *133*, 2955–2961. [CrossRef]
25. Birgisson, S.; Saha, D.; Iversen, B.B. Formation Mechanisms of Nanocrystalline MnO_2 Polymorphs under Hydrothermal Conditions. *Cryst. Growth Des.* **2018**, *18*, 827–838. [CrossRef]
26. Huang, J.; Zhong, S.; Dai, Y.; Liu, C.-C.; Zhang, H. Effect of MnO_2 Phase Structure on the Oxidative Reactivity toward Bisphenol A Degradation. *Environ. Sci. Technol.* **2018**, *52*, 11309–11318. [CrossRef] [PubMed]
27. Yang, R.; Fan, Y.; Ye, R.; Tang, Y.; Cao, X.; Yin, Z.; Zeng, Z. MnO_2-Based Materials for Environmental Applications. *Adv. Mater.* **2021**, *33*, 2004862. [CrossRef]
28. Chen, B.-R.; Sun, W.; Kitchaev, D.A.; Mangum, J.S.; Thampy, V.; Garten, L.M.; Ginley, D.S.; Gorman, B.P.; Stone, K.H.; Ceder, G.; et al. Understanding crystallization pathways leading to manganese oxide polymorph formation. *Nat. Commun.* **2018**, *9*, 2553. [CrossRef]
29. Tang, W.; Liu, L.L.; Tian, S.; Li, L.; Yue, Y.B.; Wu, Y.P.; Guan, S.Y.; Zhu, K. Nano-$LiCoO_2$ as cathode material of large capacity and high rate capability for aqueous rechargeable lithium batteries. *Electrochem. Commun.* **2010**, *12*, 1524–1526. [CrossRef]
30. Biswal, A.; Chandra Tripathy, B.; Sanjay, K.; Subbaiah, T.; Minakshi, M. Electrolytic manganese dioxide (EMD): A perspective on worldwide production, reserves and its role in electrochemistry. *RSC Adv.* **2015**, *5*, 58255–58283. [CrossRef]
31. Dose, W.M.; Donne, S.W. Heat treated electrolytic manganese dioxide for primary Li/MnO_2 batteries: Effect of manganese dioxide properties on electrochemical performance. *Electrochim. Acta* **2013**, *105*, 305–313. [CrossRef]
32. Meng, Y.; Song, W.; Huang, H.; Ren, Z.; Chen, S.-Y.; Suib, S.L. Structure–Property Relationship of Bifunctional MnO_2 Nanostructures: Highly Efficient, Ultra-Stable Electrochemical Water Oxidation and Oxygen Reduction Reaction Catalysts Identified in Alkaline Media. *J. Am. Chem. Soc.* **2014**, *136*, 11452–11464. [CrossRef] [PubMed]
33. Kitchaev, D.A.; Dacek, S.T.; Sun, W.; Ceder, G. Thermodynamics of Phase Selection in MnO_2 Framework Structures through Alkali Intercalation and Hydration. *J. Am. Chem. Soc.* **2017**, *139*, 2672–2681. [CrossRef]
34. Suib, S.L. Porous Manganese Oxide Octahedral Molecular Sieves and Octahedral Layered Materials. *Acc. Chem. Res.* **2008**, *41*, 479–487. [CrossRef]
35. Ghosh, S.K. Diversity in the Family of Manganese Oxides at the Nanoscale: From Fundamentals to Applications. *ACS Omega* **2020**, *5*, 25493–25504. [CrossRef]

36. Pistoia, G.; Antonini, A.; Zane, D.; Pasquali, M. Synthesis of Mn spinels from different polymorphs of MnO_2. *J. Power Sources* **1995**, *56*, 37–43. [CrossRef]
37. Chukhrov, F.V.; Gorshkov, A.I.; Sivtsov, A.V.; Berezovskaya, V.V.; Dikov, Y.P.; Dubinina, G.A.; Varinov, N.N. Akhtenskite—The natural analog oF ε-MnO_2. *Int. Geol. Rev.* **1989**, *31*, 1068–1072. [CrossRef]
38. Hunter, J.C. Preparation of a new crystal form of manganese dioxide: λ-MnO_2. *J. Solid State Chem.* **1981**, *39*, 142–147. [CrossRef]
39. Hendriks, R.; Cunha, D.M.; Singh, D.P.; Huijben, M. Enhanced Lithium Transport by Control of Crystal Orientation in Spinel LiMn2O4 Thin Film Cathodes. *ACS Appl. Energy Mater.* **2018**, *1*, 7046–7051. [CrossRef] [PubMed]
40. Shin, J.; Seo, J.K.; Yaylian, R.; Huang, A.; Meng, Y.S. A review on mechanistic understanding of MnO_2 in aqueous electrolyte for electrical energy storage systems. *Int. Mater. Rev.* **2020**, *65*, 356–387. [CrossRef]
41. Wang, J.; Zhao, H.; Song, J.; Zhu, T.; Xu, W. Structure-Activity Relationship of Manganese Oxide Catalysts for the Catalytic Oxidation of (chloro)-VOCs. *Catalysts* **2019**, *9*, 726. [CrossRef]
42. Dey, S.; Praveen Kumar, V. V The performance of highly active manganese oxide catalysts for ambient conditions carbon monoxide oxidation. *Curr. Res. Green Sustain. Chem.* **2020**, *3*, 100012. [CrossRef]
43. Shen, X.-F.; Ding, Y.-S.; Liu, J.; Han, Z.-H.; Budnick, J.I.; Hines, W.A.; Suib, S.L. A Magnetic Route to Measure the Average Oxidation State of Mixed-Valent Manganese in Manganese Oxide Octahedral Molecular Sieves (OMS). *J. Am. Chem. Soc.* **2005**, *127*, 6166–6167. [CrossRef]
44. Ilton, E.S.; Post, J.E.; Heaney, P.J.; Ling, F.T.; Kerisit, S.N. XPS determination of Mn oxidation states in Mn (hydr)oxides. *Appl. Surf. Sci.* **2016**, *366*, 475–485. [CrossRef]
45. Liu, J.; Zhang, Y.; Gu, Q.; Sheng, A.; Zhang, B. Tunable Mn Oxidation State and Redox Potential of Birnessite Coexisting with Aqueous Mn(II) in Mildly Acidic Environments. *Minerals* **2020**, *10*, 690. [CrossRef]
46. Bernardini, S.; Bellatreccia, F.; Della Ventura, G.; Sodo, A. A Reliable Method for Determining the Oxidation State of Manganese at the Microscale in Mn Oxides via Raman Spectroscopy. *Geostand. Geoanal. Res.* **2021**, *45*, 223–244. [CrossRef]
47. Pan, G.-H.; Song, R.-J.; Li, J.-H. Radical-mediated synthesis of γ-lactones by copper-catalyzed intermolecular carboesterification of alkenes with α-carbonyl alkyl bromides and H_2O. *Org. Chem. Front.* **2018**, *5*, 179–183. [CrossRef]
48. Wu, L.; Zhang, Z.; Liao, J.; Li, J.; Wu, W.; Jiang, H. MnO_2-promoted carboesterification of alkenes with anhydrides: A facile approach to γ-lactones. *Chem. Commun.* **2016**, *52*, 2628–2631. [CrossRef] [PubMed]
49. Ndolomingo, M.J.; Meijboom, R. Noble and Base-Metal Nanoparticles Supported on Mesoporous Metal Oxides: Efficient Catalysts for the Selective Hydrogenation of Levulinic Acid to γ-Valerolactone. *Catal. Lett.* **2019**, *149*, 2807–2822. [CrossRef]
50. Nie, J.; Liu, H. Efficient aerobic oxidation of 5-hydroxymethylfurfural to 2,5-diformylfuran on manganese oxide catalysts. *J. Catal.* **2014**, *316*, 57–66. [CrossRef]
51. Kamimura, A.; Nozaki, Y.; Ishikawa, S.; Inoue, R.; Nakayama, M. K-birnessite MnO_2: A new selective oxidant for benzylic and allylic alcohols. *Tetrahedron Lett.* **2011**, *52*, 538–540. [CrossRef]
52. Fu, X.; Feng, J.; Wang, H.; Ng, K.M. Manganese oxide hollow structures with different phases: Synthesis, characterization and catalytic application. *Catal. Commun.* **2009**, *10*, 1844–1848. [CrossRef]
53. Maji, B.; Yamamoto, H. Proline-Tetrazole-Catalyzed Enantioselective N-Nitroso Aldol Reaction of Aldehydes with In Situ Generated Nitrosocarbonyl Compounds. *Angew. Chem. Int. Ed.* **2014**, *53*, 8714–8717. [CrossRef] [PubMed]
54. Long, Y.; Ruan, L.; Lv, X.; Lv, Y.; Su, J.; Wen, Y. TG–FTIR analysis of pyrolusite reduction by major biomass components. *Chin. J. Chem. Eng.* **2015**, *23*, 1691–1697. [CrossRef]
55. Sarmah, B.; Srivastava, R.; Manjunathan, P.; Shanbhag, G.V. Green and Sustainable Tandem Catalytic Approach for Fine-Chemicals Synthesis Using Octahedral MnO_2 Molecular Sieve: Catalytic Activity versus Method of Catalyst Synthesis. *ACS Sustain. Chem. Eng.* **2015**, *3*, 2933–2943. [CrossRef]
56. Yang, Y.; Su, X.; Zhang, L.; Kerns, P.; Achola, L.; Hayes, V.; Quardokus, R.; Suib, S.L.; He, J. Intercalating MnO_2 Nanosheets With Transition Metal Cations to Enhance Oxygen Evolution. *ChemCatChem* **2019**, *11*, 1689–1700. [CrossRef]
57. Lu, F.; Huang, J.; Wu, Q.; Zhang, Y. Mixture of α-Fe_2O_3 and MnO_2 powders for direct conversion of syngas to light olefins. *Appl. Catal. A Gen.* **2021**, *621*, 118213. [CrossRef]
58. Zhao, H.; Fang, K.; Dong, F.; Lin, M.; Sun, Y.; Tang, Z. Textual properties of Cu–Mn mixed oxides and application for methyl formate synthesis from syngas. *J. Ind. Eng. Chem.* **2017**, *54*, 117–125. [CrossRef]
59. Wang, Z.; Liu, J.; Yang, Y.; Miao, S.; Shen, F. Effect of the Mechanism of H_2S on Elemental Mercury Removal Using the MnO_2 Sorbent during Coal Gasification. *Energy Fuels* **2018**, *32*, 4453–4460. [CrossRef]
60. Sherman, J.D. Synthetic zeolites and other microporous oxide molecular sieves. *Proc. Natl. Acad. Sci. USA* **1999**, *96*, 3471–3478. [CrossRef] [PubMed]
61. Auroux, A. *Molecular Sieves—Science and Technology: Acidity and Basicity*; Karge, H., Weitkamp, J., Eds.; Springer: Berlin/Heidelberg, Germany, 2006; Volume 6. [CrossRef]
62. Kresge, C.T.; Leonowicz, M.E.; Roth, W.J.; Vartuli, J.C.; Beck, J.S. Ordered mesoporous molecular sieves synthesized by a liquid-crystal template mechanism. *Nature* **1992**, *359*, 710–712. [CrossRef]
63. Corma, A. From Microporous to Mesoporous Molecular Sieve Materials and Their Use in Catalysis. *Chem. Rev.* **1997**, *97*, 2373–2420. [CrossRef]
64. Tanev, P.T.; Pinnavaia, T.J. A Neutral Templating Route to Mesoporous Molecular Sieves. *Science* **1995**, *267*, 865–867. [CrossRef]

65. Ying, J.Y.; Mehnert, C.P.; Wong, M.S. Synthesis and Applications of Supramolecular-Templated Mesoporous Materials. *Angew. Chem. Int. Ed.* **1999**, *38*, 56–77. [CrossRef]
66. Nieto, J.M.L. The selective oxidative activation of light alkanes. From supported vanadia to multicomponent bulk V-containing catalysts. *Top. Catal.* **2006**, *41*, 3–15. [CrossRef]
67. Sadakane, M.; Kodato, K.; Kuranishi, T.; Nodasaka, Y.; Sugawara, K.; Sakaguchi, N.; Nagai, T.; Matsui, Y.; Ueda, W. Molybdenum–Vanadium-Based Molecular Sieves with Microchannels of Seven-Membered Rings of Corner-Sharing Metal Oxide Octahedra. *Angew. Chem. Int. Ed.* **2008**, *47*, 2493–2496. [CrossRef]
68. Zhu, Q.; Yin, S.; Zhou, M.; Wang, J.; Chen, C.; Hu, P.; Jiang, X.; Zhang, Z.; Li, Y.; Ueda, W. Aerobic Alcohol Oxidation by a Zeolitic Octahedral Metal Oxide based on Iron Vanadomolybdates Under Mild Conditions. *ChemCatChem* **2021**, *13*, 1763–1771. [CrossRef]
69. Corma, A.; Corresa, E.; Mathieu, Y.; Sauvanaud, L.; Al-Bogami, S.; Al-Ghrami, M.S.; Bourane, A. Crude oil to chemicals: Light olefins from crude oil. *Catal. Sci. Technol.* **2017**, *7*, 12–46. [CrossRef]
70. Besnardiere, J.; Ma, B.; Torres-Pardo, A.; Wallez, G.; Kabbour, H.; González-Calbet, J.M.; Von Bardeleben, H.J.; Fleury, B.; Buissette, V.; Sanchez, C.; et al. Structure and electrochromism of two-dimensional octahedral molecular sieve h'-WO3. *Nat. Commun.* **2019**, *10*, 327. [CrossRef]
71. Corma, A.; Navarro, M.T. From micro to mesoporous molecular sieves: Adapting composition and structure for catalysis. In *Impact of Zeolites and Other Porous Materials on the New Technologies at the Beginning of the New Millennium*; Aiello, R., Giordano, G., Testa, Eds.; Elsevier: Amsterdam, The Netherlands, 2002; Volume 142, pp. 487–501, ISBN 0167-2991.
72. Martínez, C.; Corma, A. Inorganic molecular sieves: Preparation, modification and industrial application in catalytic processes. *Coord. Chem. Rev.* **2011**, *255*, 1558–1580. [CrossRef]
73. Suib, S.L. (Ed.) Introduction. In *New and Future Developments in Catalysis*; Elsevier: Amsterdam, The Netherlands, 2013; pp. ix–x, ISBN 978-0-444-53874-1.
74. Brock, S.L.; Duan, N.; Tian, Z.R.; Giraldo, O.; Zhou, H.; Suib, S.L. A Review of Porous Manganese Oxide Materials. *Chem. Mater.* **1998**, *10*, 2619–2628. [CrossRef]
75. DeGuzman, R.N.; Shen, Y.-F.; Neth, E.J.; Suib, S.L.; O'Young, C.-L.; Levine, S.; Newsam, J.M. Synthesis and Characterization of Octahedral Molecular Sieves (OMS-2) Having the Hollandite Structure. *Chem. Mater.* **1994**, *6*, 815–821. [CrossRef]
76. Suib, S.L.; Iton, L.E. Magnetic Studies of Manganese Oxide Octahedral Molecular Sieves: A New Class of Spin Glasses. *Chem. Mater.* **1994**, *6*, 429–433. [CrossRef]
77. Suib, S.L. Microporous manganese oxides. *Curr. Opin. Solid State Mater. Sci.* **1998**, *3*, 63–70. [CrossRef]
78. Tian, Z.-R.; Tong, W.; Wang, J.-Y.; Duan, N.-G.; Krishnan, V.V.; Suib, S.L. Manganese Oxide Mesoporous Structures: Mixed-Valent Semiconducting Catalysts. *Science* **1997**, *276*, 926–930. [CrossRef]
79. Shen, Y.F.; Zerger, R.P.; DeGuzman, R.N.; Suib, S.L.; McCurdy, L.; Potter, D.I.; O'Young, C.L. Manganese Oxide Octahedral Molecular Sieves: Preparation, Characterization, and Applications. *Science* **1993**, *260*, 511–515. [CrossRef] [PubMed]
80. Wasserman, S.R.; Carrado, K.A.; Yuchs, S.E.; Shen, Y.F.; Cao, H.; Suib, S.L. The structure of new synthetic manganese oxide octahedral molecular sieves. *Phys. B Condens. Matter* **1995**, *208–209*, 674–676. [CrossRef]
81. Shen, X.-F.; Ding, Y.-S.; Liu, J.; Cai, J.; Laubernds, K.; Zerger, R.P.; Vasiliev, A.; Aindow, M.; Suib, S.L. Control of Nanometer-Scale Tunnel Sizes of Porous Manganese Oxide Octahedral Molecular Sieve Nanomaterials. *Adv. Mater.* **2005**, *17*, 805–809. [CrossRef]
82. Corma, A. State of the art and future challenges of zeolites as catalysts. *J. Catal.* **2003**, *216*, 298–312. [CrossRef]
83. Férey, G. *Crystal Chemistry. From Basic to Tools for Materials Creation*; Word Scientific Publishing Company: Singapore, 2017.
84. Plug, C.M. On the relationship between the structure of $CaFe_2O_4$ and hollandite. *J. Solid State Chem.* **1982**, *41*, 23–26. [CrossRef]
85. Bursill, L.A. Structural relationships between [beta]-gallia, rutile, hollandite, psilomelane, ramsdellite and gallium titanate type structures. *Acta Crystallogr. Sect. B* **1979**, *35*, 530. [CrossRef]
86. De Guzman, R.N.; Awaluddin, A.; Shen, Y.-F.; Tian, Z.R.; Suib, S.L.; Ching, S.; O'Young, C.-L. Electrical Resistivity Measurements on Manganese Oxides with Layer and Tunnel Structures: Birnessites, Todorokites, and Cryptomelanes. *Chem. Mater.* **1995**, *7*, 1286–1292. [CrossRef]
87. Ching, S.; Krukowska, K.S.; Suib, S.L. A new synthetic route to todorokite-type manganese oxides. *Inorg. Chim. Acta* **1999**, *294*, 123–132. [CrossRef]
88. Yin, Y.-G.; Xu, W.-Q.; Shen, Y.-F.; Suib, S.L.; O'Young, C.L. Studies of Oxygen Species in Synthetic Todorokite-like Manganese Oxide Octahedral Molecular Sieves. *Chem. Mater.* **1994**, *6*, 1803–1808. [CrossRef]
89. Cerdá-Moreno, C.; Chica, A.; Keller, S.; Rautenberg, C.; Bentrup, U. Ni-sepiolite and Ni-todorokite as efficient CO_2 methanation catalysts: Mechanistic insight by operando DRIFTS. *Appl. Catal. B Environ.* **2020**, *264*, 118546. [CrossRef]
90. Fuertes, A.; Da Costa-Serra, J.F.; Chica, A. New Catalysts based on Ni-Birnessite and Ni-Todorokite for the Efficient Production of Hydrogen by Bioethanol Steam Reforming. *Energy Procedia* **2012**, *29*, 181–191. [CrossRef]
91. Bletsa, E.; Zaccone, C.; Miano, T.; Terzano, R.; Deligiannakis, Y. Natural Mn-todorokite as an efficient and green azo dye–degradation catalyst. *Environ. Sci. Pollut. Res.* **2020**, *27*, 9835–9842. [CrossRef] [PubMed]
92. Kumagai, N.; Komaba, S.; Abe, K.; Yashiro, H. Synthesis of metal-doped todorokite-type MnO_2 and its cathode characteristics for rechargeable lithium batteries. *J. Power Sources* **2005**, *146*, 310–314. [CrossRef]
93. Zhang, H.; Cao, D.; Bai, X.; Xie, H.; Liu, X.; Jiang, X.; Lin, H.; He, H. High-Cycle-Performance Aqueous Magnesium Ions Battery Capacitor Based on a Mg-OMS-1/Graphene as Cathode and a Carbon Molecular Sieves as Anode. *ACS Sustain. Chem. Eng.* **2019**, *7*, 6113–6121. [CrossRef]

94. Zhang, H.; Ye, K.; Cang, R.; Zhu, K.; Yan, J.; Cheng, K.; Wang, G.; Cao, D. The synthesis of 1×1 magnesium octahedral molecular sieve with controllable size and shape for aqueous magnesium ion battery cathode material. *J. Electroanal. Chem.* **2017**, *807*, 37–44. [CrossRef]
95. Jakubek, T.; Hudy, C.; Indyka, P.; Nowicka, E.; Golunski, S.; Kotarba, A. Effect of noble metal addition to alkali-exchanged cryptomelane on the simultaneous soot and VOC combustion activity. *Catal. Commun.* **2019**, *132*, 105807. [CrossRef]
96. Malz, R., Jr.; Kumar, R.; Garces, L.J.; Suib, S.L. Process for Preparing Ortho Substituted Phenylamines. WO2004072028A2, 26 August 2004.
97. Kumar, R.; Garces, L.J.; Son, Y.-C.; Suib, S.L.; Malz, R.E. Manganese oxide octahedral molecular sieve catalysts for synthesis of 2-aminodiphenylamine. *J. Catal.* **2005**, *236*, 387–391. [CrossRef]
98. Yang, L.; Ma, J.; Li, X.; He, G.; Zhang, C.; He, H. Improving the catalytic performance of ozone decomposition over Pd-Ce-OMS-2 catalysts under harsh conditions. *Catal. Sci. Technol.* **2020**, *10*, 7671–7680. [CrossRef]
99. Hou, J.; Li, Y.; Mao, M.; Zhao, X.; Yue, Y. The effect of Ce ion substituted OMS-2 nanostructure in catalytic activity for benzene oxidation. *Nanoscale* **2014**, *6*, 15048–15058. [CrossRef]
100. Sultana, S.; Ye, Z.; Veerapandian, S.K.P.; Löfberg, A.; De Geyter, N.; Morent, R.; Giraudon, J.-M.; Lamonier, J.-F. Synthesis and catalytic performances of K-OMS-2, Fe/K-OMS-2 and Fe-K-OMS-2 in post plasma-catalysis for dilute TCE abatement. *Catal. Today* **2018**, *307*, 20–28. [CrossRef]
101. Lin, Y.; Minghua, H.; Jvcheng, G.; Ziqin, X. Catalytic oxidation of toluene over Co-modified manganese oxide octahedral molecular sieves (OMS-2) synthesized by different methods. *IOP Conf. Ser. Mater. Sci. Eng.* **2018**, *392*, 32017. [CrossRef]
102. Yang, Y.; Huang, J.; Zhang, S.; Wang, S.; Deng, S.; Wang, B.; Yu, G. Catalytic removal of gaseous HCBz on Cu doped OMS: Effect of Cu location on catalytic performance. *Appl. Catal. B Environ.* **2014**, *150–151*, 167–178. [CrossRef]
103. Liu, Y.; Hou, J. Ce ion substitution position effect on catalytic activity of OMS-2 for benzene oxidation. *Mater. Res. Bull.* **2019**, *118*, 110497. [CrossRef]
104. Pahalagedara, L.R.; Dharmarathna, S.; King'ondu, C.K.; Pahalagedara, M.N.; Meng, Y.T.; Kuo, C.H.; Suib, S.L. Microwave-Assisted Hydrothermal Synthesis of α-MnO_2: Lattice Expansion via Rapid Temperature Ramping and Framework Substitution. *J. Phys. Chem. C* **2014**, *118*, 20363–20373. [CrossRef]
105. Shen, X.; Morey, A.M.; Liu, J.; Ding, Y.; Cai, J.; Durand, J.; Wang, Q.; Wen, W.; Hines, W.A.; Hanson, J.C.; et al. Characterization of the Fe-Doped Mixed-Valent Tunnel Structure Manganese Oxide KOMS-2. *J. Phys. Chem. C* **2011**, *115*, 21610–21619. [CrossRef]
106. Ma, J.; Wang, C.; He, H. Transition metal doped cryptomelane-type manganese oxide catalysts for ozone decomposition. *Appl. Catal. B Environ.* **2017**, *201*, 503–510. [CrossRef]
107. Zhang, Q.; Cheng, X.; Feng, X.; Qiu, G.; Tan, W.; Liu, F. Large-scale size-controlled synthesis of cryptomelane-type manganese oxide OMS-2 in lateral and longitudinal directions. *J. Mater. Chem.* **2011**, *21*, 5223–5225. [CrossRef]
108. Sabaté, F.; Jordá, J.L.; Sabater, M.J.; Corma, A. Synthesis of isomorphically substituted Ru manganese molecular sieves and their catalytic properties for selective alcohol oxidation. *J. Mater. Chem. A* **2020**, *8*, 3771–3784. [CrossRef]
109. Fan, C.; Lu, A.; Li, Y.; Wang, C. Synthesis, characterization, and catalytic activity of cryptomelane nanomaterials produced with industrial manganese sulfate. *J. Colloid Interface Sci.* **2008**, *327*, 393–402. [CrossRef]
110. Su, Y.; Wang, L.-C.; Liu, Y.-M.; Cao, Y.; He, H.-Y.; Fan, K.-N. Microwave-accelerated solvent-free aerobic oxidation of benzyl alcohol over efficient and reusable manganese oxides. *Catal. Commun.* **2007**, *8*, 2181–2185. [CrossRef]
111. Luo, Y.; Tan, W.; Suib, S.L.; Qiu, G.; Liu, F. Dissolution and phase transformation processes of hausmannite in acidic aqueous systems under anoxic conditions. *Chem. Geol.* **2018**, *487*, 54–62. [CrossRef]
112. Dharmarathna, S.; King'ondu, C.K.; Pahalagedara, L.; Kuo, C.-H.; Zhang, Y.; Suib, S.L. Manganese octahedral molecular sieve (OMS-2) catalysts for selective aerobic oxidation of thiols to disulfides. *Appl. Catal. B Environ.* **2014**, *147*, 124–131. [CrossRef]
113. Zhang, Q.; Cheng, X.; Qiu, G.; Liu, F.; Feng, X. Size-controlled synthesis and formation mechanism of manganese oxide OMS-2 nanowires under reflux conditions with KMnO4 and inorganic acids. *Solid State Sci.* **2016**, *55*, 152–158. [CrossRef]
114. Dharmarathna, S.; King'ondu, C.K.; Pedrick, W.; Pahalagedara, L.; Suib, S.L. Direct Sonochemical Synthesis of Manganese Octahedral Molecular Sieve (OMS-2) Nanomaterials Using Cosolvent Systems, Their Characterization, and Catalytic Applications. *Chem. Mater.* **2012**, *24*, 705–712. [CrossRef]
115. Tian, H.; He, J.; Zhang, X.; Zhou, L.; Wang, D. Facile synthesis of porous manganese oxide K-OMS-2 materials and their catalytic activity for formaldehyde oxidation. *Microporous Mesoporous Mater.* **2011**, *138*, 118–122. [CrossRef]
116. Yamaguchi, K.; Kobayashi, H.; Wang, Y.; Oishi, T.; Ogasawara, Y.; Mizuno, N. Green oxidative synthesis of primary amides from primary alcohols or aldehydes catalyzed by a cryptomelane-type manganese oxide-based octahedral molecular sieve, OMS-2. *Catal. Sci. Technol.* **2013**, *3*, 318–327. [CrossRef]
117. Bi, X.; Huang, Y.; Liu, X.; Yao, N.; Zhao, P.; Meng, X.; Astruc, D. Oxidative degradation of aqueous organic contaminants over shape-tunable MnO_2 nanomaterials via peroxymonosulfate activation. *Sep. Purif. Technol.* **2021**, *275*, 119141. [CrossRef]
118. Dinh, M.T.N.; Nguyen, C.C.; Phan, M.D.; Duong, M.K.; Nguyen, P.H.D.; Lancelot, C.; Nguyen, D.L. Novel cryptomelane nanosheets for the superior catalytic combustion of oxygenated volatile organic compounds. *J. Hazard. Mater.* **2021**, *417*, 126111. [CrossRef]
119. Jin, L.; Reutenauer, J.; Opembe, N.; Lai, M.; Martenak, D.J.; Han, S.; Suib, S.L. Studies on Dehydrogenation of Ethane in the Presence of CO_2 over Octahedral Molecular Sieve (OMS-2) Catalysts. *ChemCatChem* **2009**, *1*, 441–444. [CrossRef]

120. Sriskandakumar, T.; Opembe, N.; Chen, C.-H.; Morey, A.; King'ondu, C.; Suib, S.L. Green Decomposition of Organic Dyes Using Octahedral Molecular Sieve Manganese Oxide Catalysts. *J. Phys. Chem. A* **2009**, *113*, 1523–1530. [CrossRef] [PubMed]
121. Cui, J.; Wu, X.; Yang, S.; Li, C.; Tang, F.; Chen, J.; Chen, Y.; Xiang, Y.; Wu, X.; He, Z. Cryptomelane-Type KMn8O16 as Potential Cathode Material—For Aqueous Zinc Ion Battery. *Front. Chem.* **2018**, *6*, 352. [CrossRef] [PubMed]
122. Ho, P.H.; Lee, S.C.; Kim, J.; Lee, D.; Woo, H.C. Properties of a manganese oxide octahedral molecular sieve (OMS-2) for adsorptive desulfurization of fuel gas for fuel cell applications. *Fuel Process. Technol.* **2015**, *131*, 238–246. [CrossRef]
123. Poyraz, A.S.; Huang, J.; Pelliccione, C.J.; Tong, X.; Cheng, S.; Wu, L.; Zhu, Y.; Marschilok, A.C.; Takeuchi, K.J.; Takeuchi, E.S. Synthesis of cryptomelane type [small alpha]-MnO_2 (KxMn8O16) cathode materials with tunable K+ content: The role of tunnel cation concentration on electrochemistry. *J. Mater. Chem. A* **2017**, *5*, 16914–16928. [CrossRef]
124. Poyraz, A.S.; Huang, J.; Wu, L.; Bock, D.C.; Zhu, Y.; Marschilok, A.C.; Takeuchi, K.J.; Takeuchi, E.S. Potassium-Based α-Manganese Dioxide Nanofiber Binder-Free Self-Supporting Electrodes: A Design Strategy for High Energy Density Batteries. *Energy Technol.* **2016**, *4*, 1358–1368. [CrossRef]
125. Rasul, S.; Suzuki, S.; Yamaguchi, S.; Miyayama, M. Manganese oxide octahedral molecular sieves as insertion electrodes for rechargeable Mg batteries. *Electrochim. Acta* **2013**, *110*, 247–252. [CrossRef]
126. Liu, T.; Li, Q.; Xin, Y.; Zhang, Z.; Tang, X.; Zheng, L.; Gao, P.-X. Quasi free K cations confined in hollandite-type tunnels for catalytic solid (catalyst)-solid (reactant) oxidation reactions. *Appl. Catal. B Environ.* **2018**, *232*, 108–116. [CrossRef]
127. Kona, J.R.; King'ondu, C.K.; Howell, A.R.; Suib, S.L. OMS-2 for Aerobic, Catalytic, One-pot Alcohol Oxidation-Wittig Reactions: Efficient Access to α,β-Unsaturated Esters. *ChemCatChem* **2014**, *6*, 749–752. [CrossRef]
128. Ferlin, F.; Marini, A.; Ascani, N.; Ackermann, L.; Lanari, D.; Vaccaro, L. Heterogeneous Manganese-Catalyzed Oxidase C−H/C−O Cyclization to Access Pharmaceutically Active Compounds. *ChemCatChem* **2020**, *12*, 449–454. [CrossRef]
129. Opembe, N.N.; Guild, C.; King'ondu, C.; Nelson, N.C.; Slowing, I.I.; Suib, S.L. Vapor-Phase Oxidation of Benzyl Alcohol Using Manganese Oxide Octahedral Molecular Sieves (OMS-2). *Ind. Eng. Chem. Res.* **2014**, *53*, 19044–19051. [CrossRef]
130. Makwana, V.D.; Garces, L.J.; Liu, J.; Cai, J.; Son, Y.-C.; Suib, S.L. Selective oxidation of alcohols using octahedral molecular sieves: Influence of synthesis method and property–activity relations. *Catal. Today* **2003**, *85*, 225–233. [CrossRef]
131. Schurz, F.; Bauchert, J.M.; Merker, T.; Schleid, T.; Hasse, H.; Gläser, R. Octahedral molecular sieves of the type K-OMS-2 with different particle sizes and morphologies: Impact on the catalytic properties in the aerobic partial oxidation of benzyl alcohol. *Appl. Catal. A Gen.* **2009**, *355*, 42–49. [CrossRef]
132. Sabaté, F.; Navas, J.; Sabater, M.J.; Corma, A. Synthesis of γ-lactones from easily and accessible reactants catalyzed by Cu–MnOx catalysts. *C. R. Chim.* **2018**, *21*, 164–173. [CrossRef]
133. Sabaté, F.; Jordà, J.L.; Sabater, M.J. Ruthenium isomorphic substitution into Manganese Oxide Octahedral Molecular Sieve OMS-2: Comparative physic-chemical and catalytic studies of Ru versus Abundant Metal Cationic Dopants. *Catal. Today* **2021**. [CrossRef]
134. Pan, F.; Liu, W.; Yu, Y.; Yin, X.; Wang, Q.; Zheng, Z.; Wu, M.; Zhao, D.; Zhang, Q.; Lei, X.; et al. The effects of manganese oxide octahedral molecular sieve chitosan microspheres on sludge bacterial community structures during sewage biological treatment. *Sci. Rep.* **2016**, *6*, 37518. [CrossRef]
135. Yu, X.; Zhao, Z.; Wei, Y.; Liu, J. Ordered micro/macro porous K-OMS-2/SiO_2 nanocatalysts: Facile synthesis, low cost and high catalytic activity for diesel soot combustion. *Sci. Rep.* **2017**, *7*, 43894. [CrossRef]
136. Hernández, W.Y.; Centeno, M.A.; Ivanova, S.; Eloy, P.; Gaigneaux, E.M.; Odriozola, J.A. Cu-modified cryptomelane oxide as active catalyst for CO oxidation reactions. *Appl. Catal. B Environ.* **2012**, *123–124*, 27–35. [CrossRef]
137. Davó-Quiñonero, A.; Navlani-García, M.; Lozano-Castelló, D.; Bueno-López, A. CuO/cryptomelane catalyst for preferential oxidation of CO in the presence of H_2: Deactivation and regeneration. *Catal. Sci. Technol.* **2016**, *6*, 5684–5692. [CrossRef]
138. Ousmane, M.; Perrussel, G.; Yan, Z.; Clacens, J.M.; De Campo, F.; Pera-Titus, M. Highly selective direct amination of primary alcohols over a Pd/K-OMS-2 catalyst. *J. Catal.* **2014**, *309*, 439–452. [CrossRef]
139. Hou, J.; Li, Y.; Liu, L.; Ren, L.; Zhao, X. Effect of giant oxygen vacancy defects on the catalytic oxidation of OMS-2 nanorods. *J. Mater. Chem. A* **2013**, *1*, 6736–6741. [CrossRef]
140. Doménech-Carbó, A.; Sabaté, F.; Sabater, M.J. Electrochemical Analysis of Catalytic and Oxygen Interfacial Transfer Effects on MnO_2 Deposited on Gold Electrodes. *J. Phys. Chem. C* **2018**, *122*, 10939–10947. [CrossRef]
141. Davó-Quiñonero, A.; Such-Basáñez, I.; Juan-Juan, J.; Lozano-Castelló, D.; Stelmachowski, P.; Grzybek, G.; Kotarba, A.; Bueno-López, A. New insights into the role of active copper species in CuO/Cryptomelane catalysts for the CO-PROX reaction. *Appl. Catal. B Environ.* **2019**, 118372. [CrossRef]
142. Bellussi, G.; Fattore, V. Isomorphous Substitution in Zeolites: A Route for the Preparation of Novel Catalysts. In *Zeolite Chemistry and Catalysis*; Jacobs, P.A., Jaeger, N.I., Kubelková, L., Wichterlov, B., Eds.; Elsevier: Amsterdam, The Netherlands, 1991; Volume 69, pp. 79–92, ISBN 0167-2991.
143. Delgado, D.; Concepción, P.; Trunschke, A.; López Nieto, J.M. Tungsten–niobium oxide bronzes: A bulk and surface structural study. *Dalton Trans.* **2020**, *49*, 13282–13293. [CrossRef] [PubMed]
144. Gómez-Recio, I.; Azor-Lafarga, A.; Ruiz-González, M.L.; Hernando, M.; Parras, M.; Calvino, J.J.; Fernández-Díaz, M.T.; Portehault, D.; Sanchez, C.; González-Calbet, J.M. Unambiguous localization of titanium and iron cations in doped manganese hollandite nanowires. *Chem. Commun.* **2020**, *56*, 4812–4815. [CrossRef] [PubMed]
145. Cai, J.; Liu, J.; Willis, W.S.; Suib, S.L. Framework Doping of Iron in Tunnel Structure Cryptomelane. *Chem. Mater.* **2001**, *13*, 2413–2422. [CrossRef]

146. King'ondu, C.K.; Opembe, N.; Chen, C.; Ngala, K.; Huang, H.; Iyer, A.; Garcés, H.F.; Suib, S.L. Manganese Oxide Octahedral Molecular Sieves (OMS-2) Multiple Framework Substitutions: A New Route to OMS-2 Particle Size and Morphology Control. *Adv. Funct. Mater.* **2011**, *21*, 312–323. [CrossRef]
147. El-Sawy, A.M.; King'ondu, C.K.; Kuo, C.-H.; Kriz, D.A.; Guild, C.J.; Meng, Y.; Frueh, S.J.; Dharmarathna, S.; Ehrlich, S.N.; Suib, S.L. X-ray Absorption Spectroscopic Study of a Highly Thermally Stable Manganese Oxide Octahedral Molecular Sieve (OMS-2) with High Oxygen Reduction Reaction Activity. *Chem. Mater.* **2014**, *26*, 5752–5760. [CrossRef]
148. Li, W.; Cui, X.; Zeng, R.; Du, G.; Sun, Z.; Zheng, R.; Ringer, S.P.; Dou, S.X. Performance modulation of α-MnO_2 nanowires by crystal facet engineering. *Sci. Rep.* **2015**, *5*, 8987. [CrossRef]
149. Shah, S.I.; Khan, T.; Khan, R.; Khan, S.A.; Khattak, S.A.; Khan, G. Study of structural, optical and dielectric properties of α-MnO_2 nanotubes (NTS). *J. Mater. Sci. Mater. Electron.* **2019**, *30*, 19199–19205. [CrossRef]
150. Feng, Q.; Kanoh, H.; Miyai, Y.; Ooi, K. Alkali Metal Ions Insertion/Extraction Reactions with Hollandite-Type Manganese Oxide in the Aqueous Phase. *Chem. Mater.* **1995**, *7*, 148–153. [CrossRef]
151. Calvert, C.; Joesten, R.; Ngala, K.; Villegas, J.; Morey, A.; Shen, X.; Suib, S.L. Synthesis, Characterization, and Rietveld Refinement of Tungsten-Framework-Doped Porous Manganese Oxide (K-OMS-2) Material. *Chem. Mater.* **2008**, *20*, 6382–6388. [CrossRef]
152. Chen, X.; Shen, Y.-F.; Suib, S.L.; O'Young, C.L. Characterization of Manganese Oxide Octahedral Molecular Sieve (M−OMS-2) Materials with Different Metal Cation Dopants. *Chem. Mater.* **2002**, *14*, 940–948. [CrossRef]
153. Hu, R.; Cheng, Y.; Xie, L.; Wang, D. Effect of Doped Ag on Performance of Manganese Oxide Octahedral Molecular Sieve for CO Oxidation. *Chin. J. Catal.* **2007**, *28*, 463–468. [CrossRef]
154. Hu, R.; Yan, C.; Xie, L.; Cheng, Y.; Wang, D. Selective oxidation of CO in rich hydrogen stream over Ag/OMS-2 catalyst. *Int. J. Hydrog. Energy* **2011**, *36*, 64–71. [CrossRef]
155. Li, Y.; Fan, Z.; Shi, J.; Liu, Z.; Zhou, J.; Shangguan, W. Modified manganese oxide octahedral molecular sieves M′-OMS-2 (M′=Co,Ce,Cu) as catalysts in post plasma-catalysis for acetaldehyde degradation. *Catal. Today* **2015**, *256*, 178–185. [CrossRef]
156. Yue, L.; Hu, M.; Tian, M.; Liao, X.; Xu, Z.; Shi, L.; He, C. Insight Into the Role of Ceria on OMS-2 and OL Materials for Catalytic Degradation of Toluene. *Front. Environ. Chem.* **2020**, *1*, 12. [CrossRef]
157. Nur, H.; Hayati, F.; Hamdan, H. On the location of different titanium sites in Ti–OMS-2 and their catalytic role in oxidation of styrene. *Catal. Commun.* **2007**, *8*, 2007–2011. [CrossRef]
158. Chen, C.-H.; Njagi, E.C.; Chen, S.-Y.; Horvath, D.T.; Xu, L.; Morey, A.; Mackin, C.; Joesten, R.; Suib, S.L. Structural Distortion of Molybdenum-Doped Manganese Oxide Octahedral Molecular Sieves for Enhanced Catalytic Performance. *Inorg. Chem.* **2015**, *54*, 10163–10171. [CrossRef]
159. Genuino, H.C.; Meng, Y.; Horvath, D.T.; Kuo, C.H.; Seraji, M.S.; Morey, A.M.; Joesten, R.L.; Suib, S.L. Enhancement of Catalytic Activities of Octahedral Molecular Sieve Manganese Oxide for Total and Preferential CO Oxidation through Vanadium Ion Framework Substitution. *ChemCatChem* **2013**, *5*, 2306–2317. [CrossRef]
160. Polverejan, M.; Villegas, J.C.; Suib, S.L. Higher Valency Ion Substitution into the Manganese Oxide Framework. *J. Am. Chem. Soc.* **2004**, *126*, 7774–7775. [CrossRef]
161. Legutko, P.; Gryboś, J.; Fedyna, M.; Janas, J.; Wach, A.; Szlachetko, J.; Adamski, A.; Yu, X.; Zhao, Z.; Kotarba, A.; et al. Soot Combustion over Niobium-Doped Cryptomelane (K-OMS-2) Nanorods—Redox State of Manganese and the Lattice Strain Control the Catalysts Performance. *Catalysts* **2020**, *10*, 1390. [CrossRef]
162. Wasalathanthri, N.D.; Guild, C.; Nizami, Q.A.; Dissanayake, S.L.; He, J.; Kerns, P.; Fee, J.; Achola, L.; Rathnayake, D.; Weerakkody, C.; et al. Niobium-substituted octahedral molecular sieve (OMS-2) materials in selective oxidation of methanol to dimethoxymethane. *RSC Adv.* **2019**, *9*, 32665–32673. [CrossRef]
163. Luo, J.; Zhang, Q.; Garcia-Martinez, J.; Suib, S.L. Adsorptive and Acidic Properties, Reversible Lattice Oxygen Evolution, and Catalytic Mechanism of Cryptomelane-Type Manganese Oxides as Oxidation Catalysts. *J. Am. Chem. Soc.* **2008**, *130*, 3198–3207. [CrossRef] [PubMed]
164. Özacar, M.; Poyraz, A.S.; Genuino, H.C.; Kuo, C.-H.; Meng, Y.; Suib, S.L. Influence of silver on the catalytic properties of the cryptomelane and Ag-hollandite types manganese oxides OMS-2 in the low-temperature CO oxidation. *Appl. Catal. A Gen.* **2013**, *462–463*, 64–74. [CrossRef]
165. Dutov, V.V.; Mamontov, G.V.; Sobolev, V.I.; Vodyankina, O.V. Silica-supported silver-containing OMS-2 catalysts for ethanol oxidative dehydrogenation. *Catal. Today* **2016**, *278*, 164–173. [CrossRef]
166. Chen, J.; Li, J.; Li, H.; Huang, X.; Shen, W. Facile synthesis of Ag–OMS-2 nanorods and their catalytic applications in CO oxidation. *Microporous Mesoporous Mater.* **2008**, *116*, 586–592. [CrossRef]
167. Qu, Z.; Bu, Y.; Qin, Y.; Wang, Y.; Fu, Q. The improved reactivity of manganese catalysts by Ag in catalytic oxidation of toluene. *Appl. Catal. B Environ.* **2013**, *132–133*, 353–362. [CrossRef]
168. O'Donnell, R.; Ralphs, K.; Grolleau, M.; Manyar, H.; Artioli, N. Doping Manganese Oxides with Ceria and Ceria Zirconia Using a One-Pot Sol–Gel Method for Low Temperature Diesel Oxidation Catalysts. *Top. Catal.* **2020**, *63*, 351–362. [CrossRef]
169. Wang, R.; Li, J. OMS-2 Catalysts for Formaldehyde Oxidation: Effects of Ce and Pt on Structure and Performance of the Catalysts. *Catal. Lett.* **2009**, *131*, 500–505. [CrossRef]
170. Xie, J.; Chen, L.; Zhou, W.-F.; Au, C.-T.; Yin, S.-F. Selective oxidation of p-chlorotoluene to p-chlorobenzaldehyde over metal-modified OMS-2 molecular sieves. *J. Mol. Catal. A Chem.* **2016**, *425*, 110–115. [CrossRef]

171. Chen, J.; Wang, W.; Zhai, S.; Sun, P.; Wu, Z. The positive effect of Ca2+ on cryptomelane-type octahedral molecular sieve (K-OMS-2) catalysts for chlorobenzene combustion. *J. Colloid Interface Sci.* **2020**, *576*, 496–504. [CrossRef] [PubMed]
172. Yu, L.; Diao, G.; Ye, F.; Sun, M.; Zhou, J.; Li, Y.; Liu, Y. Promoting Effect of Ce in Ce/OMS-2 Catalyst for Catalytic Combustion of Dimethyl Ether. *Catal. Lett.* **2011**, *141*, 111–119. [CrossRef]
173. Santos, V.P.; Soares, O.S.G.P.; Bakker, J.J.W.; Pereira, M.F.R.; Órfão, J.J.M.; Gascon, J.; Kapteijn, F.; Figueiredo, J.L. Structural and chemical disorder of cryptomelane promoted by alkali doping: Influence on catalytic properties. *J. Catal.* **2012**, *293*, 165–174. [CrossRef]
174. Santos, V.P.; Carabineiro, S.A.C.; Bakker, J.J.W.; Soares, O.S.G.P.; Chen, X.; Pereira, M.F.R.; Órfão, J.J.M.; Figueiredo, J.L.; Gascon, J.; Kapteijn, F. Stabilized gold on cerium-modified cryptomelane: Highly active in low-temperature CO oxidation. *J. Catal.* **2014**, *309*, 58–65. [CrossRef]
175. Adjimi, S.; García-Vargas, J.M.; Díaz, J.A.; Retailleau, L.; Gil, S.; Pera-Titus, M.; Guo, Y.; Giroir-Fendler, A. Highly efficient and stable Ru/K-OMS-2 catalyst for NO oxidation. *Appl. Catal. B Environ.* **2017**, *219*, 459–466. [CrossRef]
176. Molleti, J.; Tiwari, M.S.; Yadav, G.D. Novel synthesis of Ru/OMS catalyst by solvent-free method: Selective hydrogenation of levulinic acid to γ-valerolactone in aqueous medium and kinetic modelling. *Chem. Eng. J.* **2018**, *334*, 2488–2499. [CrossRef]
177. Chen, S.; Huang, H.; Jiang, P.; Yang, K.; Diao, J.; Gong, S.; Liu, S.; Huang, M.; Wang, H.; Chen, Q. Mn-Doped RuO_2 Nanocrystals as Highly Active Electrocatalysts for Enhanced Oxygen Evolution in Acidic Media. *ACS Catal.* **2020**, *10*, 1152–1160. [CrossRef]
178. Xu, Y.-F.; Chen, Y.; Xu, G.-L.; Zhang, X.-R.; Chen, Z.; Li, J.-T.; Huang, L.; Amine, K.; Sun, S.-G. RuO_2 nanoparticles supported on MnO_2 nanorods as high efficient bifunctional electrocatalyst of lithium-oxygen battery. *Nano Energy* **2016**, *28*, 63–70. [CrossRef]
179. Ishikawa, M.; Tamura, M.; Nakagawa, Y.; Tomishige, K. Demethoxylation of guaiacol and methoxybenzenes over carbon-supported Ru–Mn catalyst. *Appl. Catal. B Environ.* **2016**, *182*, 193–203. [CrossRef]
180. Yang, L.; Ma, J.; Li, X.; Zhang, C.; He, H. Enhancing Oxygen Vacancies of Ce-OMS-2 via Optimized Hydrothermal Conditions to Improve Catalytic Ozone Decomposition. *Ind. Eng. Chem. Res.* **2020**, *59*, 118–128. [CrossRef]
181. Ahrens, L.H. The use of ionization potentials Part 1. Ionic radii of the elements. *Geochim. Cosmochim. Acta* **1952**, *2*, 155–169. [CrossRef]
182. Hayati, F.; Chandren, S.; Hamdan, H.; Nur, H. The Role of Ti and Lewis Acidity in Manganese Oxide Octahedral Molecular Sieves Impregnated with Titanium in Oxidation Reactions. *Bull. Chem. React. Eng. Catal.* **2014**, *9*, 28–38. [CrossRef]
183. Gao, T.; Glerup, M.; Krumeich, F.; Nesper, R.; Fjellvåg, H.; Norby, P. Microstructures and Spectroscopic Properties of Cryptomelane-type Manganese Dioxide Nanofibers. *J. Phys. Chem. C* **2008**, *112*, 13134–13140. [CrossRef]
184. Tabassum, L.; Tasnim, H.; Meguerdichian, A.G.; Willis, W.S.; Macharia, J.; Price, C.; Dang, Y.; Suib, S.L. Enhanced Catalytic Activity of a Vanadium-Doped Mesoporous Octahedral Molecular Sieve-2 (K-OMS-2) toward Hydrogen Evolution Reaction. *ACS Appl. Energy Mater.* **2020**, *3*, 12185–12193. [CrossRef]
185. Hecht, D.S.; Hu, L.; Irvin, G. Emerging Transparent Electrodes Based on Thin Films of Carbon Nanotubes, Graphene, and Metallic Nanostructures. *Adv. Mater.* **2011**, *23*, 1482–1513. [CrossRef] [PubMed]
186. Minami, T. Chapter Five—Transparent Conductive Oxides for Transparent Electrode Applications. In *Oxide Semiconductors*; Svensson, B.G., Pearton, S.J., Jagadish, C., Eds.; Elsevier: Amsterdam, The Netherlands, 2013. [CrossRef]
187. Bae, S.; Kim, H.; Lee, Y.; Xu, X.; Park, J.-S.; Zheng, Y.; Balakrishnan, J.; Lei, T.; Ri Kim, H.; Song, Y.I.; et al. Roll-to-roll production of 30-inch graphene films for transparent electrodes. *Nat. Nanotechnol.* **2010**, *5*, 574–578. [CrossRef]
188. Liu, Z.; Xing, Y.; Chen, C.-H.; Zhao, L.; Suib, S.L. Framework Doping of Indium in Manganese Oxide Materials: Synthesis, Characterization, and Electrocatalytic Reduction of Oxygen. *Chem. Mater.* **2008**, *20*, 2069–2071. [CrossRef]
189. Wu, X.; Yu, X.; Chen, Z.; Huang, Z.; Jing, G. Low-valence or tetravalent cation doping of manganese oxide octahedral molecular sieve (K-OMS-2) materials for nitrogen oxide emission abatement. *Catal. Sci. Technol.* **2019**, *9*, 4108–4117. [CrossRef]
190. Nguyen Dinh, M.T.; Giraudon, J.M.; Vandenbroucke, A.M.; Morent, R.; De Geyter, N.; Lamonier, J.F. Manganese oxide octahedral molecular sieve K-OMS-2 as catalyst in post plasma-catalysis for trichloroethylene degradation in humid air. *J. Hazard. Mater.* **2016**, *314*, 88–94. [CrossRef] [PubMed]
191. Wang, C.; Ma, J.; Liu, F.; He, H.; Zhang, R. The Effects of Mn^{2+} Precursors on the Structure and Ozone Decomposition Activity of Cryptomelane-Type Manganese Oxide (OMS-2) Catalysts. *J. Phys. Chem. C* **2015**, *119*, 23119–23126. [CrossRef]
192. Tseng, L.-T.; Lu, Y.; Fan, H.M.; Wang, Y.; Luo, X.; Liu, T.; Munroe, P.; Li, S.; Yi, J. Magnetic properties in α-MnO_2 doped with alkaline elements. *Sci. Rep.* **2015**, *5*, 9094. [CrossRef] [PubMed]
193. Li, X.; Ma, J.; He, H. Recent advances in catalytic decomposition of ozone. *J. Environ. Sci.* **2020**, *94*, 14–31. [CrossRef] [PubMed]
194. Dotsenko, S.S.; Verkhov, V.A.; Svetlichnyi, V.A.; Liotta, L.F.; La Parola, V.; Izaak, T.I.; Vodyankina, O. V Oxidative dehydrogenation of ethanol on modified OMS-2 catalysts. *Catal. Today* **2020**, *357*, 503–510. [CrossRef]
195. Makwana, V.D.; Son, Y.-C.; Howell, A.R.; Suib, S.L. The Role of Lattice Oxygen in Selective Benzyl Alcohol Oxidation Using OMS-2 Catalyst: A Kinetic and Isotope-Labeling Study. *J. Catal.* **2002**, *210*, 46–52. [CrossRef]
196. Gu, Y.; Min, Y.; Li, L.; Lian, Y.; Sun, H.; Wang, D.; Rummeli, M.H.; Guo, J.; Zhong, J.; Xu, L.; et al. Crystal Splintering of β-MnO_2 Induced by Interstitial Ru Doping Toward Reversible Oxygen Conversion. *Chem. Mater.* **2021**, *33*, 4135–4145. [CrossRef]
197. Kwon, N.H.; Lee, K.-G.; Kim, H.K.; Hwang, S.-J. MnO_2-based nanostructured materials for various energy applications. *Mater. Chem. Front.* **2021**, *5*, 3549–3575. [CrossRef]

198. Garcia, C.; Truttmann, V.; Lopez, I.; Haunold, T.; Marini, C.; Rameshan, C.; Pittenauer, E.; Kregsamer, P.; Dobrezberger, K.; Stöger-Pollach, M.; et al. Dynamics of Pd Dopant Atoms inside Au Nanoclusters during Catalytic CO Oxidation. *J. Phys. Chem. C* **2020**, *124*, 23626–23636. [CrossRef]
199. López-Hernández, I.; García, C.; Truttmann, V.; Pollitt, S.; Barrabés, N.; Rupprechter, G.; Rey, F.; Palomares, A.E. Evaluation of the silver species nature in Ag-ITQ2 zeolites by the CO oxidation reaction. *Catal. Today* **2020**, *345*, 22–26. [CrossRef]
200. Sarma, B.B.; Plessow, P.N.; Agostini, G.; Concepción, P.; Pfänder, N.; Kang, L.; Wang, F.R.; Studt, F.; Prieto, G. Metal-Specific Reactivity in Single-Atom Catalysts: CO Oxidation on 4d and 5d Transition Metals Atomically Dispersed on MgO. *J. Am. Chem. Soc.* **2020**, *142*, 14890–14902. [CrossRef] [PubMed]
201. Liu, L.; Corma, A. Metal Catalysts for Heterogeneous Catalysis: From Single Atoms to Nanoclusters and Nanoparticles. *Chem. Rev.* **2018**, *118*, 4981–5079. [CrossRef] [PubMed]
202. Royer, S.; Duprez, D. Catalytic Oxidation of Carbon Monoxide over Transition Metal Oxides. *ChemCatChem* **2011**, *3*, 24–65. [CrossRef]
203. Fu, Z.; Chen, M.; Ye, Q.; Dong, N.; Dai, H. Enhanced Performance of the OMS-2-Supported CuOx Catalysts for Carbon Monoxide, Ethyl Acetate, and Toluene Oxidation. *Catalysts* **2021**, *11*, 713. [CrossRef]
204. Chen, J.; Tang, X.; Liu, J.; Zhan, E.; Li, J.; Huang, X.; Shen, W. Synthesis and Characterization of Ag−Hollandite Nanofibers and Its Catalytic Application in Ethanol Oxidation. *Chem. Mater.* **2007**, *19*, 4292–4299. [CrossRef]
205. Li, L.; King, D.L. Synthesis and Characterization of Silver Hollandite and Its Application in Emission Control. *Chem. Mater.* **2005**, *17*, 4335–4343. [CrossRef]
206. Genuino, H.C.; Seraji, M.S.; Meng, Y.; Valencia, D.; Suib, S.L. Combined experimental and computational study of CO oxidation promoted by Nb in manganese oxide octahedral molecular sieves. *Appl. Catal. B Environ.* **2015**, *163*, 361–369. [CrossRef]
207. Genuino, H.C.; Valencia, D.; Suib, S.L. Insights into the structure–property–activity relationship in molybdenum-doped octahedral molecular sieve manganese oxides for catalytic oxidation. *Catal. Sci. Technol.* **2018**, *8*, 6493–6502. [CrossRef]
208. Jiang, Z.; Ma, Y.; Li, Y.; Liu, H. Highly effective UV–Vis-IR and IR photothermocatalytic CO abatement on Zn doped OMS-2 nanorods. *Appl. Surf. Sci.* **2019**, *483*, 827–834. [CrossRef]
209. Davó-Quiñonero, A.; Lozano-Castelló, D.; Bueno-López, A. Unexpected stability of CuO/Cryptomelane catalyst under Preferential Oxidation of CO reaction conditions in the presence of CO_2 and H_2O. *Appl. Catal. B Environ.* **2017**, *217*, 459–465. [CrossRef]
210. He, J.; Chen, S.-Y.; Tang, W.; Dang, Y.; Kerns, P.; Miao, R.; Dutta, B.; Gao, P.-X.; Suib, S.L. Microwave-assisted integration of transition metal oxide nanocoatings on manganese oxide nanoarray monoliths for low temperature CO oxidation. *Appl. Catal. B Environ.* **2019**, *255*, 117766. [CrossRef]
211. Stelmachowski, P.; Monteverde Videla, A.H.A.; Jakubek, T.; Kotarba, A.; Specchia, S. The Effect of Fe, Co, and Ni Structural Promotion of Cryptomelane (KMn8O16) on the Catalytic Activity in Oxygen Evolution Reaction. *Electrocatalysis* **2018**, *9*, 762–769. [CrossRef]